minerals

MDPI

Article

Genesis of the Halılar Metasediment-Hosted Cu-Pb (±Zn) Mineralization, NW Turkey: Evidence from Mineralogy, Alteration, and Sulfur Isotope Geochemistry

Demet Kiran Yildirim

Department of Geological Engineering, Faculty of Mines, Istanbul Technical University, 34469 Istanbul, Turkey; kirand@itu.edu.tr

Abstract: This study contributes to our understanding of the evolution of Halılar Cu-Pb (±Zn) mineralization (NW Turkey) based on mineralogical and geochemical results and sulfur isotope data. The study area represents local Cu-Pb with some Zn brecciated-stockwork vein type mineralization along the NE–SW fault gouge zone at the lower boundary of the Sakarkaya and Düztarla granitoid rocks. Two main zones, consisting of sericite–quartz–chlorite ± kaolinite ± pyrite (i.e., zone-1) and calcite–epidote–albite ± chlorite ± sericite (i.e., zone-2), were observed within the central ore mineral zone at the mining site. Different mineralization assemblages were recorded; the main ore mineral contains chalcopyrite, galena, pyrite, and sphalerite within alteration zone-1, and the oxidation/supergene mineralization includes covellite and goethite. The mass balance calculations show that the samples of zone-1 show an increase in SiO_2, Fe_2O_3, K_2O, and LOI along with Ag, As, Cu, Mo, Pb, S, Sb, and Zn, reflecting high pyritization with sericitization and silicification. On the other hand, the samples from zone-2 are rich in CaO; Na_2O; P_2O_5; TiO_2; LOI; and carbon-reflecting calcite, epidote, and albite alterations. A uniform magmatic sulfur source of Halılar sulfides is suggested by their mean $\delta^{34}S$ value of −1.62‰. Furthermore, the primary metal source is metasediments and intrusive Düztarla granitoid magmatism. These observations suggest that the Halılar metasediment-hosted Cu-Pb (±Zn) mineralization was formed by epigenetic hydrothermal processes after sedimentation/diagenesis and metamorphism.

Keywords: mass-balance calculations; $\delta^{34}S$ data; Cu-Pb (±Zn) mineralization; Halılar; NW Turkey

Citation: Yildirim, D.K. Genesis of the Halılar Metasediment-Hosted Cu-Pb (±Zn) Mineralization, NW Turkey: Evidence from Mineralogy, Alteration, and Sulfur Isotope Geochemistry. *Minerals* **2022**, *12*, 991. https://doi.org/10.3390/min12080991

Academic Editor: Yuichi Morishita

Received: 6 July 2022
Accepted: 31 July 2022
Published: 4 August 2022

1. Introduction

Studies of hydrothermal alteration are important in the exploration of copper deposits in order to determine the processes of ore formation, as well as to identify potential ore zones [1]. Spectroscopic methods, geophysics, or multispectral remote sensing techniques are used in mapping alteration zones, as well as in identifying their mineral assemblages [1–9]. In addition, the geochemical changes from host rock to alteration zones provide alteration type and its degree, as well as the genesis and evolution of the hydrothermal system [5,10–19]. Hydrothermal alteration processes are responsible for mineralogical and chemical changes in the rock-forming minerals as a result of interactions between the hydrothermal fluids and host rocks along fracture zones and grain boundaries [1,2,20,21]. Schwartz [22] stated that the alteration generally depends on: (1) temperature, pressure, and chemical composition of the fluid; (2) the chemical and physical nature of the wall rocks; and (3) the water–rock ratio. The mechanism and types of mineral deposits are assigned by the nature of the alteration assemblages and the different hydrothermal systems. In addition, the mineral assemblages of the altered rocks are important to help identify the alteration types (e.g., phyllic alteration refers to assemblages of quartz + sericite + pyrite minerals; potassic alteration: orthoclase + biotite + sericite; propylitic alteration: epidote + chlorite + albite) [23]. Gifkins et al. [24] defined different types of mineral deposits by

their alteration type and mineralogy, such as porphyry Cu deposits having potassic, phyllic, argillic, and propylitic alterations, while the low-sulfidation, epithermal, geothermal, VHMS, and sediment-hosted massive sulphide deposits having sericitic (or phyllic) and propylitic (or saussuritization) alterations.

In Turkey, mineralization in the structural zone of the Anatolian tectonic belt represents part of the Tethyan–Eurasian metallogenic belt (TEMB), which formed during the Mesozoic and Early Cenozoic [25]. This mineralization was controlled by extensional events that formed after the Neo-Tethys closure. It is associated with calc–alkaline magmatic activity during the Oligocene–Miocene/Pliocene within the post-collision continent-continent environments and led to the formation of Pb-Zn, Sb, As, and Au-Cu deposits [25].

The study area (Halılar area) is located about 25–30 km northeast of Edremit in Balıkesir Province (Biga Peninsula, Turkey) (Figure 1). Halılar Cu-Pb (±Zn) mineralization occurs in a vein-type deposit that formed in the volcanogenic metasediments of the Sakarkaya Formation. It is associated with the NE–SW fault gouge zone along with the lower boundary of the Bağcağız Formation and the Düztarla granitoid intrusion.

Although geological and geochemical studies of the Halılar area have been published [26], the genesis of base-metal Cu-Pb (-Zn) mineralization in this area remains ambiguous, as it has not been studied in detail. Therefore, this study focuses on mineralization in the Halılar area by reporting new data obtained from mineralogical, petrographical, and geochemical investigations of the mineralization and altered host rock. Using mass balance calculations, enrichment and/or depletion in the chemical components of the different alteration zones associated with this mineralization were calculated on the basis of their mass/volume changes (gain and loss). Sulfur isotope data from the sulfide minerals, including pyrite, chalcopyrite, and galena, were collected to understand the sulfur source(s), as well as to determine the $\delta^{34}S_{H2S}$ values of the hydrothermal fluid that caused the Halılar Cu-Pb-(±Zn) mineralization.

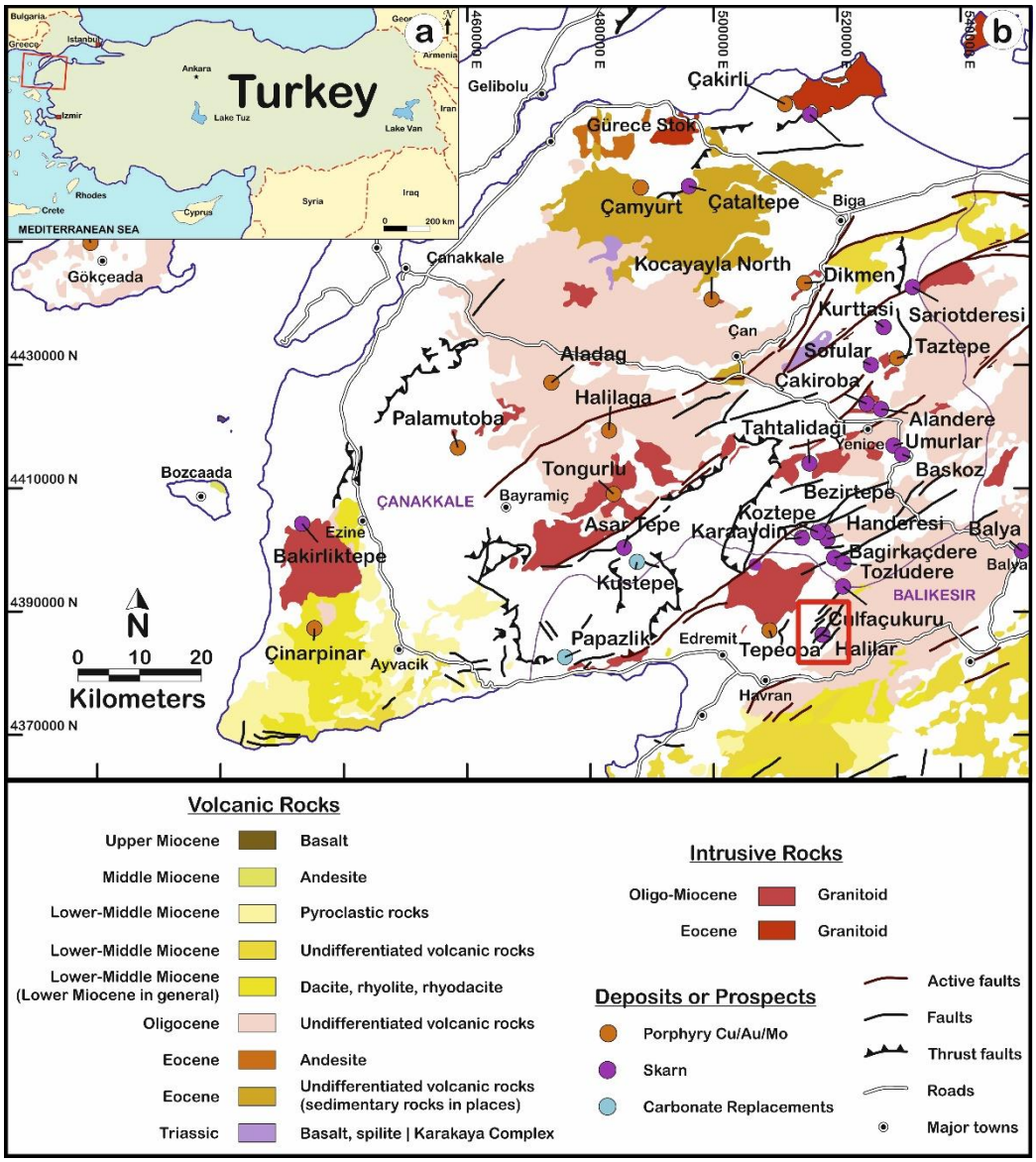

Figure 1. (**a**) Geological map of Turkey; (**b**) study area around Halılar in the Northeast of Edremit in Balıkesir after Yigit [27].

2. Geological Setting

The Halılar area contains two groups: the clastic Halılar Group, which is slightly metamorphosed and overlain by the pre-Late Triassic age or Permian limestone [28], and the Bilecik group. These two groups are in contact with the intrusive rocks to the N and NW of Halılar village (Figure 2). The Halılar Group consists of two formations: the Bağcağız and Sakarkaya Formations; the Bilecik Group is represented by two formations: the Taşçıbayırı Formation and Günören Limestone (Figure 2). The granitoid rocks intruded the Sakarkaya and Bağcağız Formations of the Halılar Group in the study area (Figure 2).

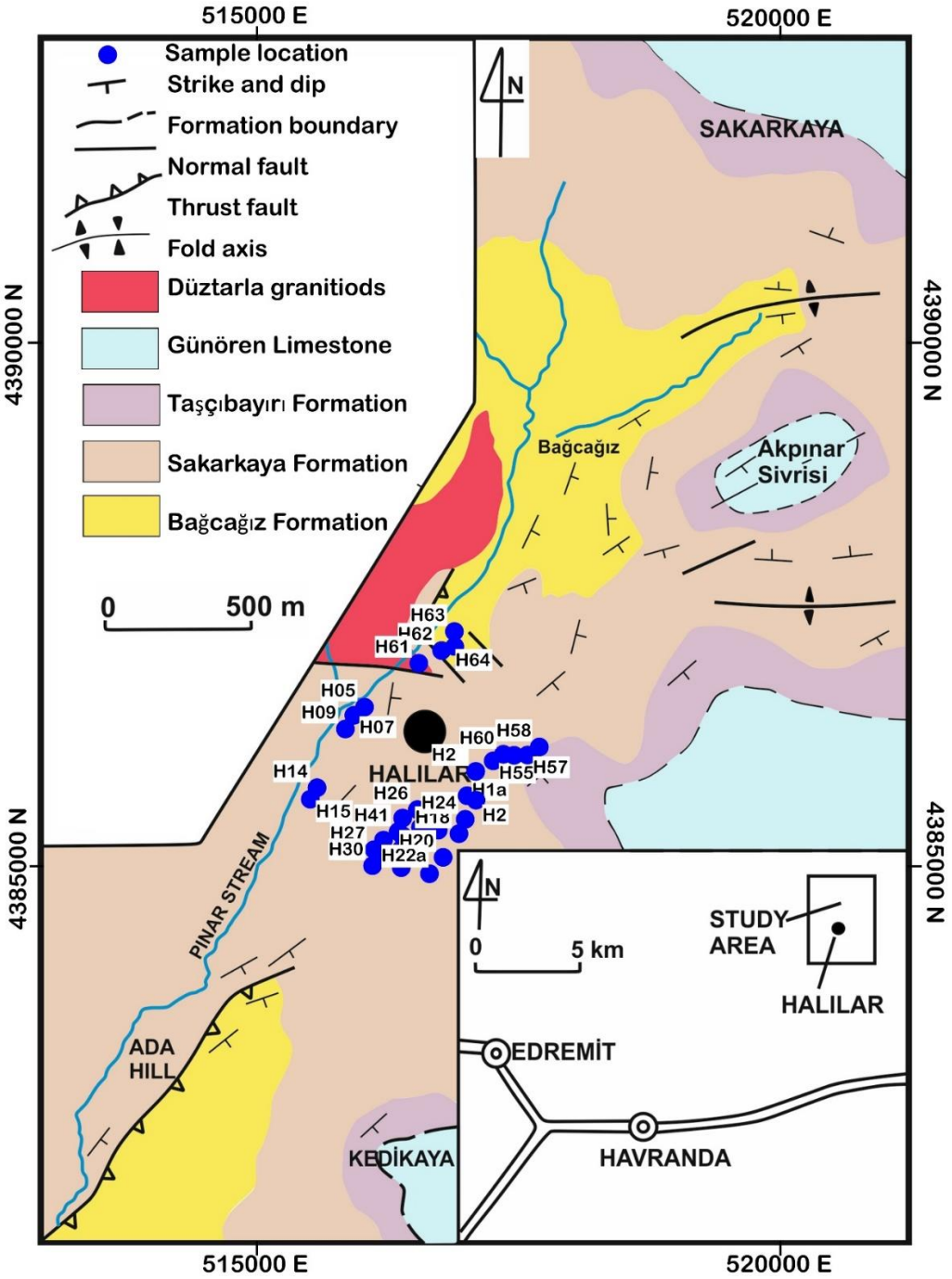

Figure 2. Geologic map of the Halılar area after Altiner et al. [26].

The Halılar Group was classified by Krushensky, Akcay, and Karaege [28] into the Bağcağız Formation (sandstone and shale) and the Sakarkaya Formation (sandstone and conglomerate). The Bağcağız Formation (sample IDs: H63 and H64) was intruded by the Düztarla granitoid at its lower boundary (Figure 2). It has dark siltstone at its upper boundary, which is overlain by the sandstone of the Sakarkaya Formation. This formation also has sandstone and siltstone alternations from bottom to top, consisting of dark-grayish-colored siltstones and silty shales with yellowish-colored, medium-bedded sandstones from the Lower Triassic to Middle Jurassic. The Bağcağız Formation is represented by carbonaceous dark metasiltstone and rhyolitic metatuffs (Figure 3a). The rhyolitic metatuffs are fine-grained light gray to yellowish rocks (Figure 3a) microscopically consisting of microp-

erthite and quartz crystals embedded in a finer-grained tuffaceous matrix of kaolinitized and carbonatized feldspar, quartz, and Fe-oxide (Figure 3b).

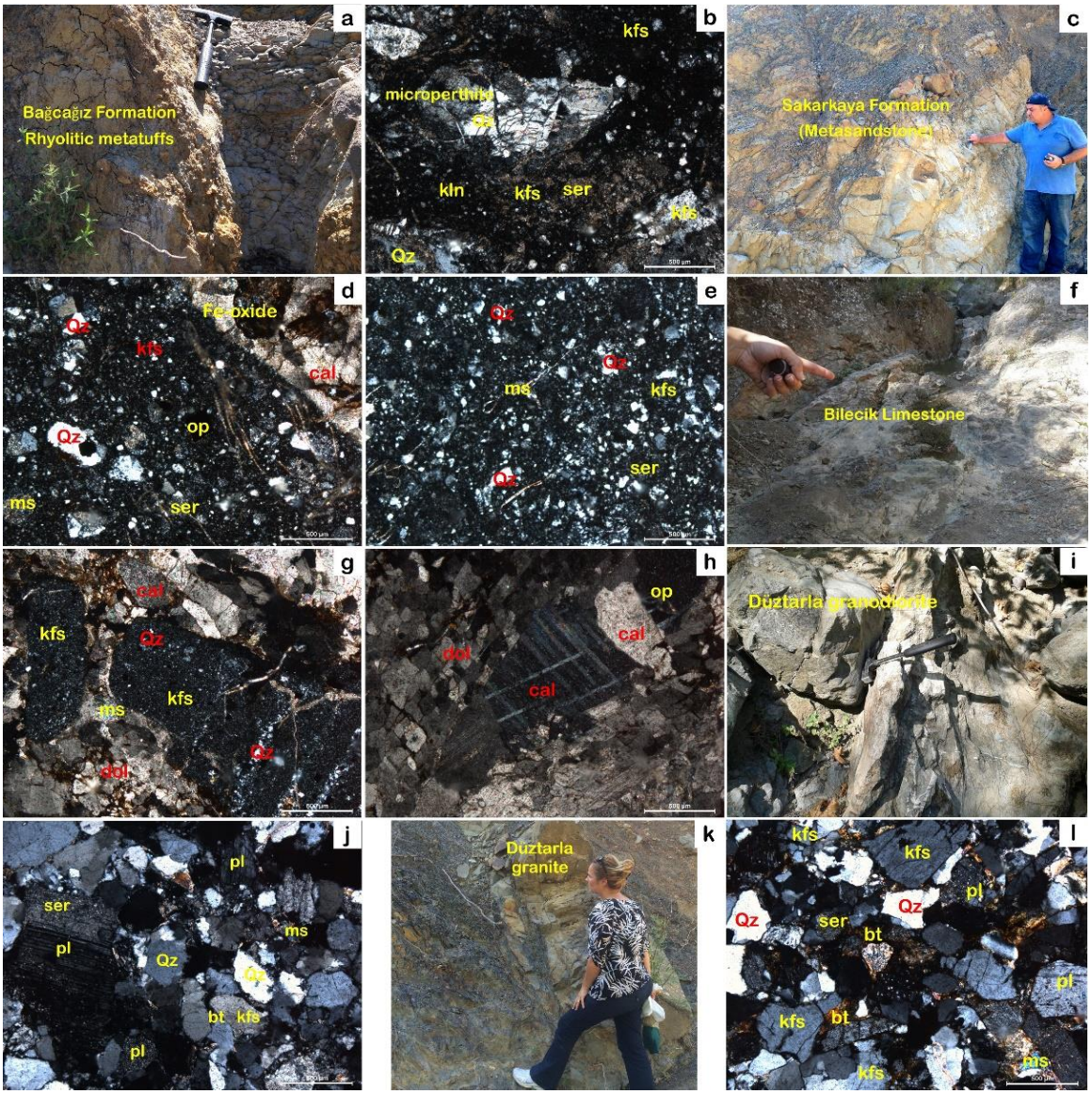

Figure 3. (**a**) Rhyolitic metatuffs of the Bağcağız Formation; (**b**) XPL photomicrograph of the mineral composition of rhyolitic metatuffs; (**c**) yellowish-colored metasandstone of the Sakarkaya Formation; (**d**,**e**) XPL photomicrograph of the poorly sorted quartz, feldspar, and mica grains bounded by iron oxide in the subarkosic-to-quartz arenitic of the metasandstone; (**f**) general view of the Bilecik Limestone; (**g**) XPL photomicrograph of the calcite with feldspar, mica, and volcanic rock fragments in the sandy limestone of the Taşçıbayırı Formation; (**h**) XPL photomicrograph of the calcite and dolomite with Fe-oxide minerals in Günören dolomitic limestone; (**i**) granodiorite of Düztarla intrusive rocks; (**j**) XPL photomicrograph of the oligoclase, quartz, and microperthite with subordinate amount of biotite and Fe-oxide minerals in granodiorite; (**k**) granite from the Düztarla intrusion invaded into the Bağcağız Formation; (**l**) XPL photomicrograph of the mineral composition of the Düztarla granite intrusion. Abbreviations: biotite (bt), calcite (cal), dolomite (dol), K-feldspar (kfs), kaolinite (kln), muscovite (ms), opaque (opq), plagioclase (pl), quartz (qz), and sericite (ser).

The Sakarkaya Formation (sample IDs: H05, H07, H09, H14, H15, H18, H20, H22a, H55, and H60) outcrops approximately 500 m south of Sakarkaya Hill and 1.5–2 km north and northeast of Halılar village (Figure 2). It is represented by fine-grained, yellowish-

colored metasandstone (Figure 3c). It has a sharp contact with the dark metasiltstones of the Bağcağız Formation. The unit rests with a distinct contact on the Bositra-bearing dark silty shale of the Bağcağız Formation [26]. The metasandstone ranges from subarkosic to wackes in composition and consists of poorly sorted quartz, sericitized and kaolinitized feldspar, and mica grains cemented by iron oxide (Figure 3d,e). These components are embedded in altered feldspar and silicified fine-grained matrix (Figure 3d,e). The upper portion of the formation is represented by cross-stratified beds.

The Bilecik Group is part of the Callovian–Hauterivian (Middle Jurassic–Lower Cretaceous) stratigraphy in NW Anatolia known as the Bilecik Limestone (Figure 3f–h). It has been divided into the two formations; Taşçıbayırı and Günören Limestone formations. The Taşçıbayırı Formation (sample IDs: H56, H57, and H58) underlies the Günören Limestone (sample ID: H59); they contain sandy limestone and dolomitic limestone, respectively. The sandy limestone of the Taşçıbayırı Formation is composed of calcite with feldspar, mica, and volcanic rock fragments (Figure 3g). The volcanic rock fragments are composed of broken and/or eroded volcanic rocks consisting of quartz and feldspar (Figure 3g), while the Günören dolomitic limestone consists of calcite and dolomite with Fe-oxide minerals (Figure 3h).

The Düztarla granitoid rocks (sample IDs: H61 and H62) reflect Upper Oligocene–Lower Miocene post-collisional magmatic activity in the study area (Figure 2), differentiated into granodiorite and granitic rocks (Figure 3i–l). The granodiorite consists of plagioclase (oligoclase in composition; 35–50 vol.%), quartz (20–35 vol.%), and microperthite (8–17 vol.%) with subordinate amounts of biotite and Fe-oxide minerals (Figure 3j). The plagioclase is slightly affected by sericite and kaolinite alteration (Figure 3j). The granite is composed of microperthite (30–45 vol.%), quartz (20–35 vol.%), and plagioclase (albite in composition; 20–30 vol.%) with muscovite and Fe-oxide minerals (Figure 3l).

The Halılar area has a well-described Upper Triassic–Liassic continuous succession (Figures 1 and 2). The tectonic sedimentary rocks formed at the Sakarya divergent margin, which evolved in the Late Triassic–Aptian interval [29,30]. As a result of the diachronic closure of the Tethys basin in western Anatolian, the Upper Triassic black shales were deposited in the Lias in the Karakaya euxinic basin throughout the Edremit region. This shale and the Hettangian arkosic sandstones were later intruded by the Düztarla granodioritic–granitic body due to the southward subduction of the Paleo-Tethys [29].

3. Sampling and Analytical Methods

A total of 45 host rocks, altered rocks, and mineralized samples were collected from the study area. Thin sections and a subset of polished sections were examined optically using transmitted and reflected light microscopes. Whole-rock major, trace, and rare earth element analyses were conducted at the Geochemistry Research Laboratories of Istanbul Technical University (ITU/JAL). The samples were grounded using a tungsten carbide milling device. Major elements were analyzed using a BRUKER S8 TIGER model X-ray fluorescence spectrometer (XRF) (Östliche Rheinbrückenstraße 49, 76187 Karlsruhe, Germany) with a wavelength range from 0.01–12 nm. Trace elements were analyzed by inductively coupled plasma-mass spectrometry (ICP-MS) using an ELAN DRC-e Perkin Elmer model (PerkinElmer, Waltham, MA, US). Approximately 100 mg of powdered sample was digested in two steps. The first step was completed with 6 mL of 37% HCl, 2 mL of 65% HNO_3, and 1 mL of 38%–40% HF in a pressure- and temperature-controlled Teflon beaker using a Berghoff Microwave™ at an average temperature of 180 °C. The second step was completed with the addition of 6 mL of 5% boric acid solution. The remaining solution sample was analyzed by ICP-MS. The altered rocks were also analyzed for mineralogy using a BRUKER X-ray diffractometer (XRD) (Östliche Rheinbrückenstraße 49, 76187 Karlsruhe, Germany). Calculation of the normative mineral abundances from the major element analyses and rare earth element diagrams were created using Igpet 2.3 [31]. The GEOISO-Windows of Coelho [32] were used to determine the absolute mobility of the elements using equations from Gresens [33] and isocon diagrams from Grant [34,35].

Sulfide minerals for sulfur isotope analysis were separated from slightly crushed (200 mesh) lode samples (>95 % pure pyrite, chalcopyrite, and galena). They were washed and handpicked under a binocular microscope. These analyses were carried out at the Geochron Laboratory (USA) using EA-IRMS (Elemental Analysis-Isotope Ratio Mass Spectrometry) techniques. All stable isotope data are reported in the delta (δ) notation, relative to Vienna-Canyon Diablo Troilite (V-CDT) for sulfur isotopes with 0.5‰ (1 σ) analytical uncertainty.

4. Halılar Cu-Pb (±Zn) Mineralization

The Halılar base metal mineralization represents Cu-Pb with some Zn brecciated-stockwork-veining-type mineralization. The mineralization is restricted to a fault gouge zone directed NE–SW, as well as along the lower boundary of the Sakarkaya and Düztarla granitoid rocks (Figure 2). It is also closely associated with intense hydrothermal alteration within the breccia and quartz stockwork veining (Figure 4a–d). Based on the field investigation and petrographic and mineralogical (XRD) data, the mineralized quartz veins and brecciated ore bodies are accompanied by two types of hydrothermal alteration zone with gradational boundaries: zone-1 (sericite–quartz–chlorite ± kaolinite ± pyrite) and zone-2 (calcite–epidote–albite ± chlorite ± sericite).

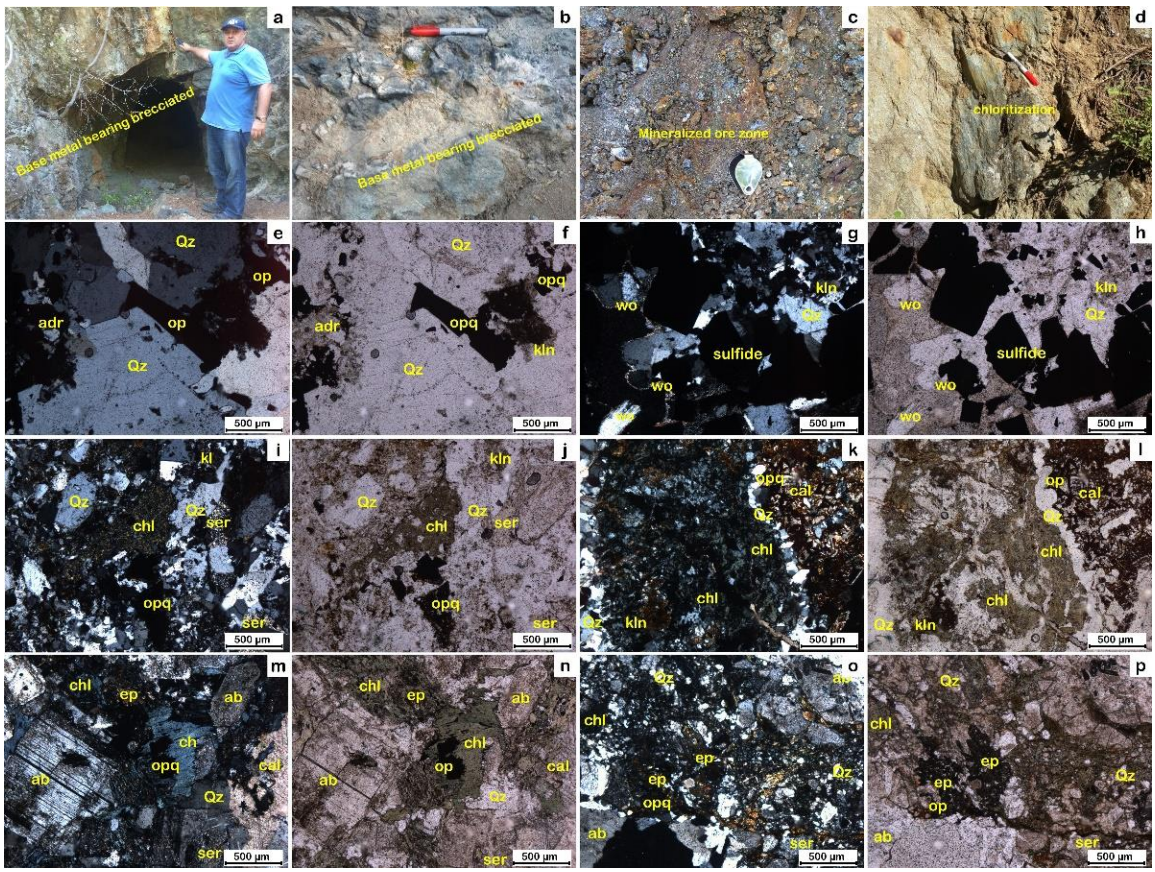

Figure 4. (**a**,**b**) Brecciation and quartz stockwork veining along with intense hydrothermal alteration; (**c**) base -metal-bearing brecciated zone; (**d**) pervasive chlorite and epidote alteration in the host rock; (**e**–**h**) XPL and PPL photomicrographs of alteration zone-1 containing quartz, wollastonite, kaolinite, and andradite with calcite in a mineralized and brecciated quartz vein; (**i**–**l**) XPL and PPL photomicrographs of alteration zone-2 with a high amount of sericite, quartz, chlorite, kaolinite, and opaque minerals; (**m**–**p**) XPL and PPL photomicrographs of the calcite, epidote, albite, and quartz with chlorite in alteration zone-2. Abbreviations: calcite (cal), chlorite (chl), epidote (ep), kaolinite (kln), opaque (opq), quartz (qz), sericite (ser), and wollastonite (wo).

The ore zone is represented by mineralized and brecciated quartz stockwork veining (Figure 4a–c). It has high amounts of Cu (9.9 %), Pb (11.3 %), and Zn (0.29 %) mineralization, with high amounts of chalcopyrite and galena with sphalerite and pyrite (Figure 4a–c). It contains quartz with a subordinate amount of wollastonite, kaolinite, andradite, and calcite (Figures 4e–h and 5 and Appendix A). These calc–silicate assemblages refer to the skarn that resulted from the metasomatism of sandy limestone in the Taşçıbayırı Formation in association with andradite (Figures 4e–h and 5 and Appendix A). The XRD data show quartz (low), wollastonite (1A, manganoan), kaolinite (1A), microcline, calcite, chalcopyrite, andradite, anglesite, and cubanite (high) with smaller amounts of pyrite, sphalerite (ferrous), galena, and quartz (high) (Figure 5 and Appendix A).

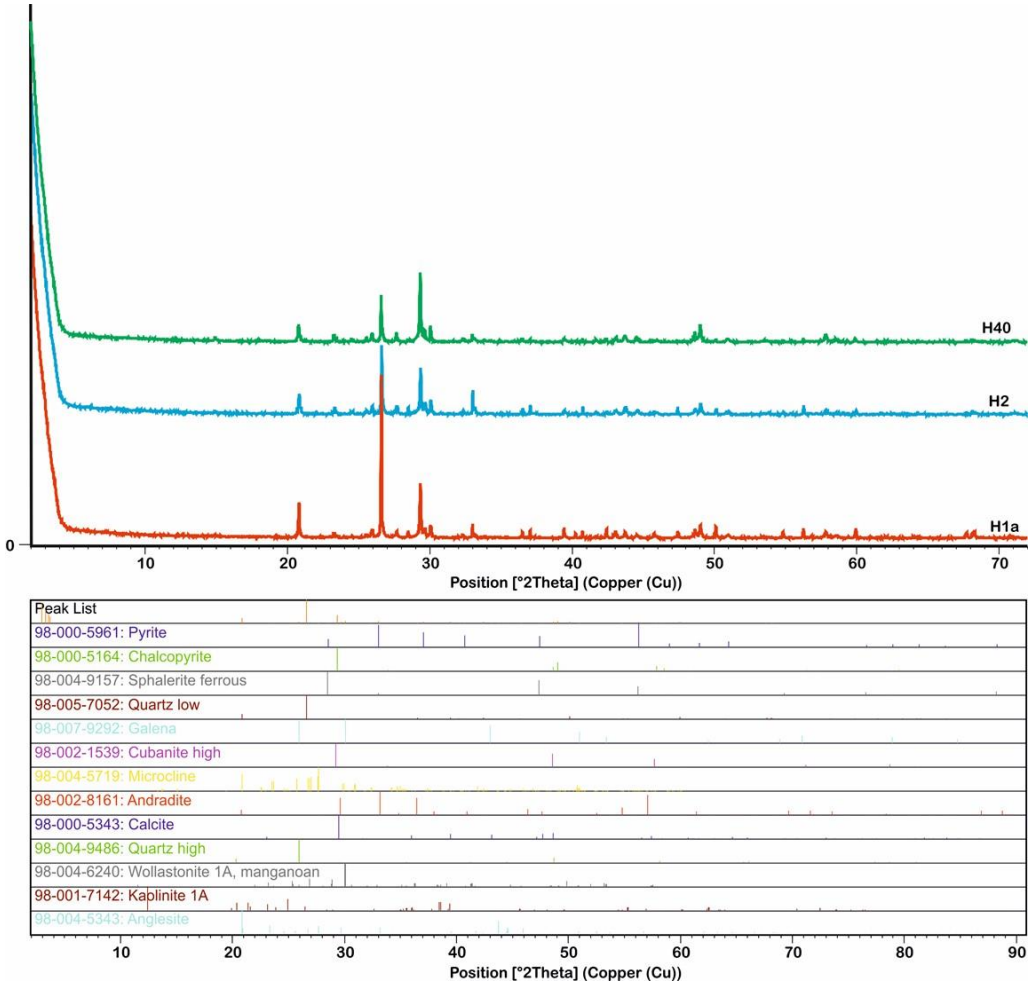

Figure 5. XRD patterns of the representative samples from the ore zone, having quartz; wollastonite; kaolinite; microcline; calcite; chalcopyrite; andradite; anglesite; and cubanite with pyrite, sphalerite, galena.

4.1. Hydrothermal Alteration Types

The hydrothermal alterations associated with Cu-Pb-Zn mineralization include extensive silicification (Figure 4e–h), sulfidation (Figure 4e–h), and carbonatization (Figure 4k–n), with some chloritization (Figure 4i–p), sericitization (Figure 4i–p), and calc–silicate alteration (Figure 4e–p) distributed in two alteration zones around the mineralized orebodies.

Alteration zone-1 (sericite–quartz–chlorite ± kaolinite ± pyrite) forms the main alteration zone developed outwards from the ore zone and has high amounts of sericite and quartz, with lesser amounts of chlorite, kaolinite, and pyrite (Figures 4i–l and 6 and Appendix B). It is characterized by the preferential replacement of the original K-feldspar and/or plagioclase–biotite by sericite/muscovite–kaolinite. XRD studies reveal a paragene-

sis of quartz (low), kaolinite (1A), clinochlore (1MIa), and sericite (2M1) with a subordinate amount of chamosite (1MIIb), pyrite, and chalcopyrite (Figure 6, Appendix B).

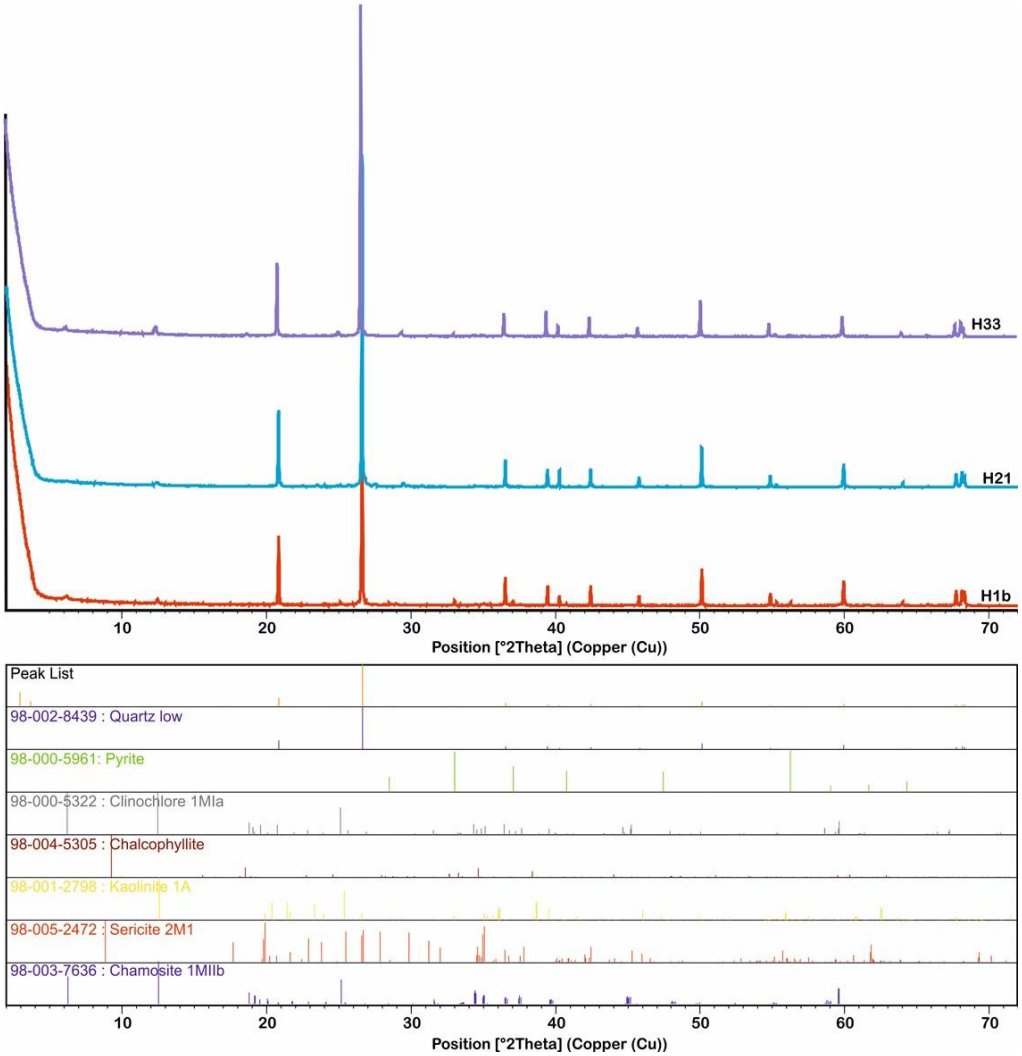

Figure 6. XRD patterns of representative samples from alteration zone-1 (sericite–quartz–chlorite ± kaolinite ± pyrite).

Alteration zone-2 (calcite–epidote–albite ± chlorite ± sericite) represents the distal zone and has higher amounts of calcite, epidote, and albite, with a subordinate amount of chlorite (Figures 4m–p and 7 and Appendix C). The sulfide minerals are less abundant in this zone (Figure 4d). The XRD data reveal that this alteration zone consists of quartz (low), albite (low), muscovite (2M1), clinochlore (IIb-4), microcline, sericite (2M1), and calcite, with lesser amounts of orthoclase, chamosite (1MIIb), and epidote (Figure 7 and Appendix C).

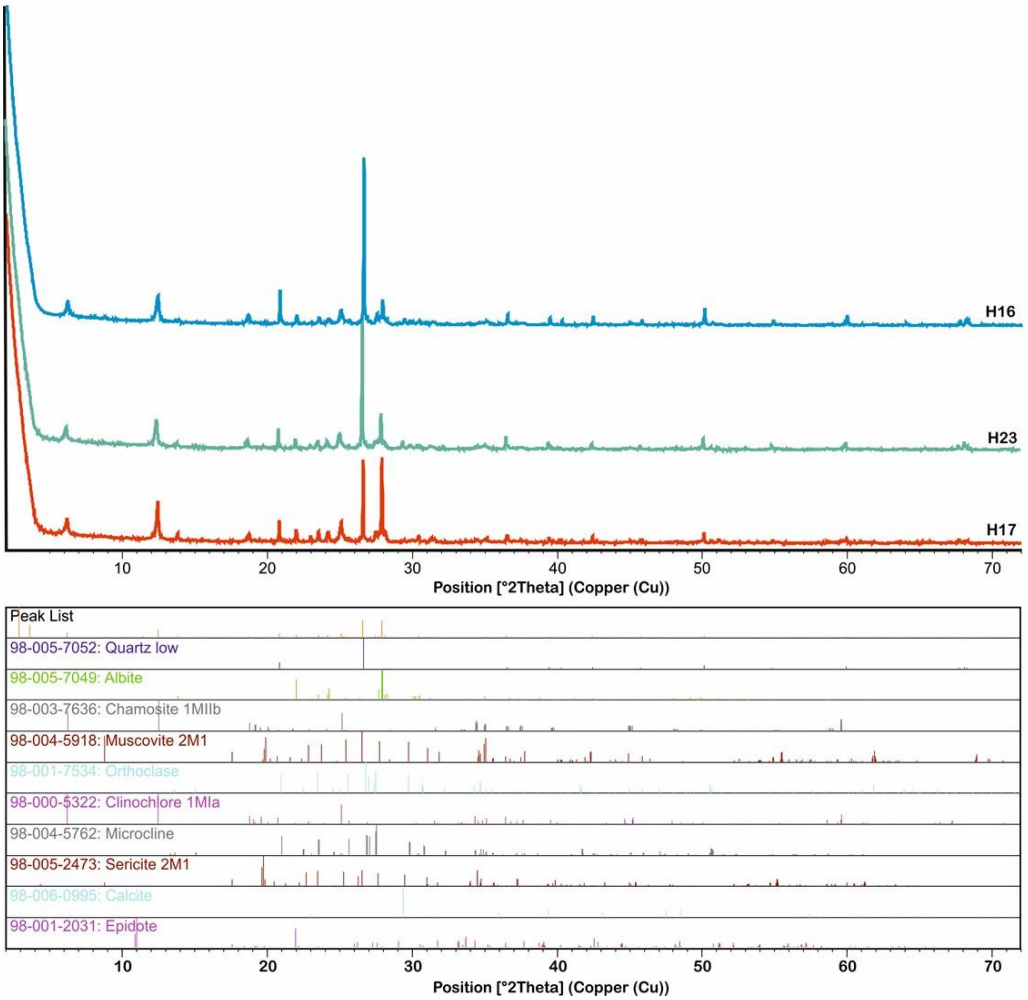

Figure 7. XRD patterns of representative samples from alteration zone-2 (calcite–epidote–albite ± chlorite ± sericite).

4.2. Ore Mineralogy

The ore mineral assemblage includes chalcopyrite, galena, pyrite, and sphalerite with covellite and goethite in abundant gangue minerals such as quartz, sericite, chlorite, and calcite forming along the quartz stockwork veins as well as in the brecciated ore zones (Figures 4–7 and Appendices A–C). Chalcopyrite and galena are the most common sulfide minerals in the ore bodies, occurring as yellow and whitish gray in color and with a subhedral granular texture (up to 2 mm), respectively (Figure 8a,b). Pyrite is either associated with or occurs as inclusions in chalcopyrite (Figure 8c,d). Sphalerite is characterized by dark gray coloring associated with chalcopyrite and pyrite, forming exsolution textures produced by chalcopyrite (Figure 8b,c,e). These minerals were developed in the main ore mineralization phase (Figure 9). On the other hand, the oxidation and supergene mineralization events represent the second phase of mineralization, including covellite and goethite formed after chalcopyrite and pyrite, respectively (Figures 8 and 9).

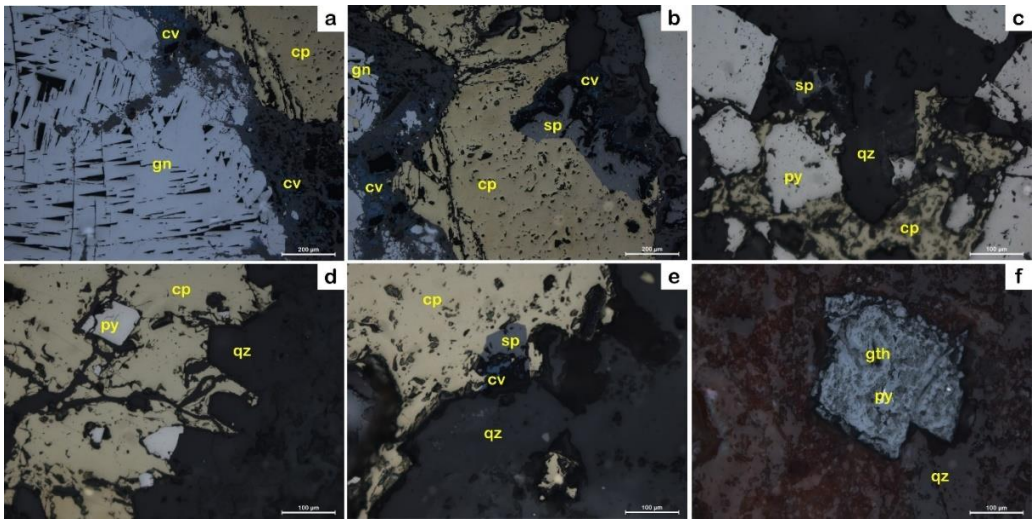

Figure 8. PPL photomicrographs of reflected light microscopy. (**a**) Galena with triangular cleavage pits associated with chalcopyrite replaced by covellite. (**b**) Chalcopyrite with sphalerite, galena, pyrite, and covellite. (**c**–**e**) Pyrite associated with chalcopyrite and sphalerite in a mineralized quartz vein. (**f**) Goethite, the main alteration product after pyrite. Abbreviations: chalcopyrite (cp), covellite (cv), galena (gn), goethite (gth), pyrite (py), quartz (qz), and sphalerite (sp).

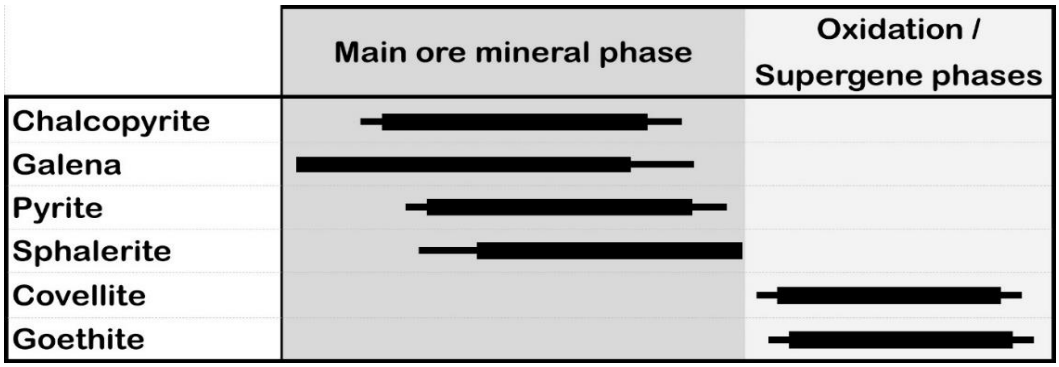

Figure 9. Paragenetic sequence of mineralization phases in the Halılar area.

5. Geochemical Characteristics

5.1. Geochemistry of the Least-Altered Metasediments

Ten representative samples collected from the least-altered metasediments of the Sakarkaya Formation were analyzed for major, trace, and rare-earth element contents (Table 1). Samples from the metasandstones are classified as mainly wackes and, rarely, Fe-sand and Fe-shale based on the geochemical classification of the terrigenous sandstones and shales by Herron [36] (Figure 10a). The samples have SiO_2/Al_2O_3 ratios ranging from 2.7 to 5.5 with an average of 4.3, which are similar to upper continental crust (UCC) [37] (~4.3 SiO_2/Al_2O_3 ratio), suggesting that they were sourced from the crustal felsic rocks. It also appears in Figure 10b,c that the Sakarkaya metasediments have acidic/intermediate characteristics, which lie mostly in the field of the metavolcanic tuffs, metagreywackes, and arkosic sands [38] according to their low K/Rb ratios (mean = 312.8). In the F1-F2 classification diagram (Figure 10d), the metasediments are mostly comparable with the compositional characteristics of the P4-quartoze sedimentary provenance that form within the passive and active continental margins (Figure 10e) due to recycling from old sedimentary rocks derived from highly weathered felsic terrains. The metasandstones have low total rare earth element contents (∑REE) (up to 145.14 ppm with an average of 88.96 ppm), ∑REE/∑HREE = 6.59–10.43 ppm, $(La/Yb)_N$ = 5.38–14.29 ppm, and positive Eu anomaly

(Eu/Eu* = 0.68–1.27 ppm) that are similar to the upper continental crust (UCC) of Taylor and McLennan [37] (Figure 10f).

Table 1. The major oxides and trace and rare-earth elements (REE) of metasediments in the Sakarkaya Formation.

Major Oxide (%)	H05	H07	H09	H-14	H-15	H-18	H-20	H-22a	H55	H60
SiO_2	59.2	62.3	67.6	68.2	50.2	64.0	58.9	63.5	65.2	61.0
Al_2O_3	14.0	13.7	16.4	16.2	18.4	13.6	14.6	11.5	13.6	15.1
Fe_2O_3	6.8	5.0	3.5	3.4	10.9	5.0	6.9	11.3	4.9	5.8
MgO	5.6	4.0	1.5	1.5	9.2	4.0	5.7	4.8	4.2	5.5
CaO	1.7	0.2	0.5	0.3	0.6	2.5	1.7	0.1	2.6	0.3
Na_2O	2.1	0.9	1.8	1.8	3.3	2.5	2.1	0.8	2.5	2.0
K_2O	4.7	3.9	5.5	5.8	1.0	4.8	4.8	1.6	4.9	4.8
TiO_2	0.6	0.6	0.5	0.5	0.7	0.5	0.7	0.3	0.8	0.4
P_2O_5	0.1	0.1	0.1	0.1	0.2	0.1	0.2	0.1	0.1	0.2
MnO	0.1	0.2	0.1	0.1	0.3	0.1	0.2	0.3	0.1	0.1
Cr_2O_3	0.0	0.1	0.0	0.0	0.1	0.0	0.0	0.0	0.0	0.0
LOI	3.2	3.9	3.6	1.8	5.0	2.6	3.8	4.0	3.5	3.4
Trace and Rare Earth Elements (ppm)										
Ag	6.7	10.7	6.0	1.7	11.7	9.7	2.3	7.0	4.6	6.8
As	19.7	17.9	222.7	33.5	24.6	14.9	21.0	424.3	222.0	18.8
Au	0.0	0.0	0.0	0.1	0.0	0.0	0.0	0.1	0.0	0.1
Ba	465.2	336.5	823.3	773.2	157.2	515.7	1130.9	381.5	756.2	423.4
Be	1.7	2.6	4.3	1.7	1.7	3.5	5.1	1.5	3.3	1.6
C	2520.7	1234.1	1284.5	545.6	708.1	2621.5	2419.9	48.2	1877.4	1259.3
Cd	0.4	0.8	1.0	0.4	0.4	1.2	0.9	1.3	1.1	0.9
Co	31.9	22.3	23.8	16.3	43.7	20.1	24.4	23.3	27.6	27.1
Cs	5.0	4.1	3.6	6.6	3.7	3.9	6.1	2.2	4.6	3.9
Cu	40.8	42.9	27.8	16.8	64.8	20.9	34.6	125.7	80.2	83.3
Ga	32.8	26.4	36.1	39.2	26.4	26.4	45.8	26.0	35.9	29.4
Hf	1.6	1.2	1.1	0.6	1.3	1.4	1.8	0.6	1.4	1.2
In	0.0	0.0	0.0	0.0	0.1	0.0	0.1	0.0	0.0	0.0
Ir	0.0	0.0	0.0	0.0	0.0	0.0	0.0	0.0	0.0	0.0
Li	67.7	83.5	63.7	16.2	119.3	47.8	79.6	104.8	92.2	86.2
Mo	2.5	2.5	2.5	1.0	2.0			3.0	2.8	2.6
Ni	42.7	37.7	37.9	32.0	53.4	22.0	53.7	45.1	49.4	43.9
Pb	232.5	272.3	306.4	33.8	101.4	54.1	61.5	911.8	356.9	416.0
Pd	1.1	1.6	1.7	0.8	1.5	1.7	1.7	0.7	1.2	0.9
Pt	0.0	0.0	0.0	0.0	0.0	0.0	0.1	0.0	0.0	0.0
Rb	122.5	92.3	107.4	125.3	46.6	149.1	182.9	62.1	99.8	103.6
Rh	0.0	0.0	0.0	0.0	0.0	0.0	0.0	0.0	0.0	0.0
Ru	0.0	0.0	0.0	0.0	0.0	0.0	0.0	0.0	0.0	0.0
S	265.1	167.7	540.9	342.1	188.1	147.4	934.3	871.9	265.1	167.7
Sb	1.5	1.7	1.6	2.0	1.3	1.1	2.1	5.3	1.8	1.6
Sn	1.8	1.4	1.6	3.3	2.3	3.6	2.5	1.1	1.5	2.2
Sr	272.1	208.3	153.9	60.3	122.8	163.3	380.8	35.7	240.2	181.1
Te	0.0	0.0	0.0	0.0	0.1	0.0	0.0	0.1	0.0	0.0
Tl	0.7	0.9	1.8	1.0	0.4	1.5	2.2	0.9	1.5	0.8
U										
Zn	420.0	500.9	460.5	197.4	72.4	270.4	258.1	581.9	480.7	470.6
Se	0.3	−0.2	3.2	0.2	1.8	-1.2	0.8	5.6	3.0	1.2
Sc	152.8	165.4	138.8	129.5	176.1	154.6	123.0	144.8	133.9	148.8
Y	18.9	11.9	12.0	7.3	8.7	19.1	18.8	5.1	15.4	12.0
La	16.0	22.5	20.4	9.8	12.0	26.1	29.6	5.7	17.1	14.7
Ce	34.6	39.7	56.3	43.0	26.1	53.2	59.3	10.6	35.0	22.6
Pr	4.0	2.6	3.3	2.3	2.6	5.8	6.8	1.2	2.9	3.1
Nd	13.6	19.4	17.7	8.5	9.9	22.5	26.0	4.6	14.7	12.6
Sm	5.3	3.5	3.3	2.3	2.2	4.9	5.8	1.3	4.4	3.4
Eu	1.4	1.3	1.5	0.9	0.6	1.6	1.5	0.4	1.0	1.1

Table 1. *Cont.*

Major Oxide (%)	H05	H07	H09	H-14	H-15	H-18	H-20	H-22a	H55	H60
Gd	3.4	4.0	4.1	2.6	2.9	6.0	5.8	1.3	4.5	3.5
Tb	0.2	0.3	0.3	0.3	0.3	0.6	0.7	0.2	0.2	0.2
Dy	1.7	3.3	3.3	1.7	2.0	3.5	3.9	1.1	1.1	3.7
Ho	0.3	0.4	0.8	0.3	0.4	0.7	0.8	0.2	0.2	0.8
Er	1.0	1.2	2.1	1.0	1.2	2.1	2.4	0.7	2.3	0.7
Tm	0.1	0.2	0.3	0.1	0.2	0.3	0.3	0.1	0.3	0.1
Yb	1.0	1.1	1.9	1.0	1.1	1.8	2.2	0.6	2.1	0.7
Lu	0.2	0.2	0.3	0.2	0.2	0.3	0.3	0.1	0.3	0.1
Th	7.6	12.0	12.3	6.8	3.9	12.6	12.7	2.1	12.0	6.9
Parameters										
K/Rb	317.8	350.0	428.3	382.1	169.1	266.2	216.7	209.3	406.0	382.8
F1	−8.6	−8.1	−5.2	−5.6	−3.8	−7.0	−8.5	−2.8	−7.8	−9.0
F2	−3.1	−4.6	2.7	3.0	−12.1	0.1	−3.2	−10.8	0.2	−3.4
K wt%	3.9	3.2	4.6	4.8	0.8	4.0	4.0	1.3	4.1	4.0
log SiO_2/Al_2O_3	0.6	0.7	0.6	0.6	0.4	0.7	0.6	0.7	0.7	0.6
log Fe_2O_3/K_2O	0.2	0.1	−0.2	−0.2	1.1	0.0	0.2	0.9	0.0	0.1
Σ REE	82.8	99.6	115.4	74.0	61.6	129.3	145.1	28.1	86.3	67.2
Σ REE/Σ HREE	10.4	9.4	8.9	10.3	7.5	8.5	8.9	6.6	7.7	6.9
Eu/Eu*	1.0	1.1	1.3	1.1	0.8	0.9	0.8	1.0	0.7	1.0
$(La/Yb)_N$	11.0	14.1	7.2	6.7	7.5	9.4	9.0	6.0	5.4	14.3

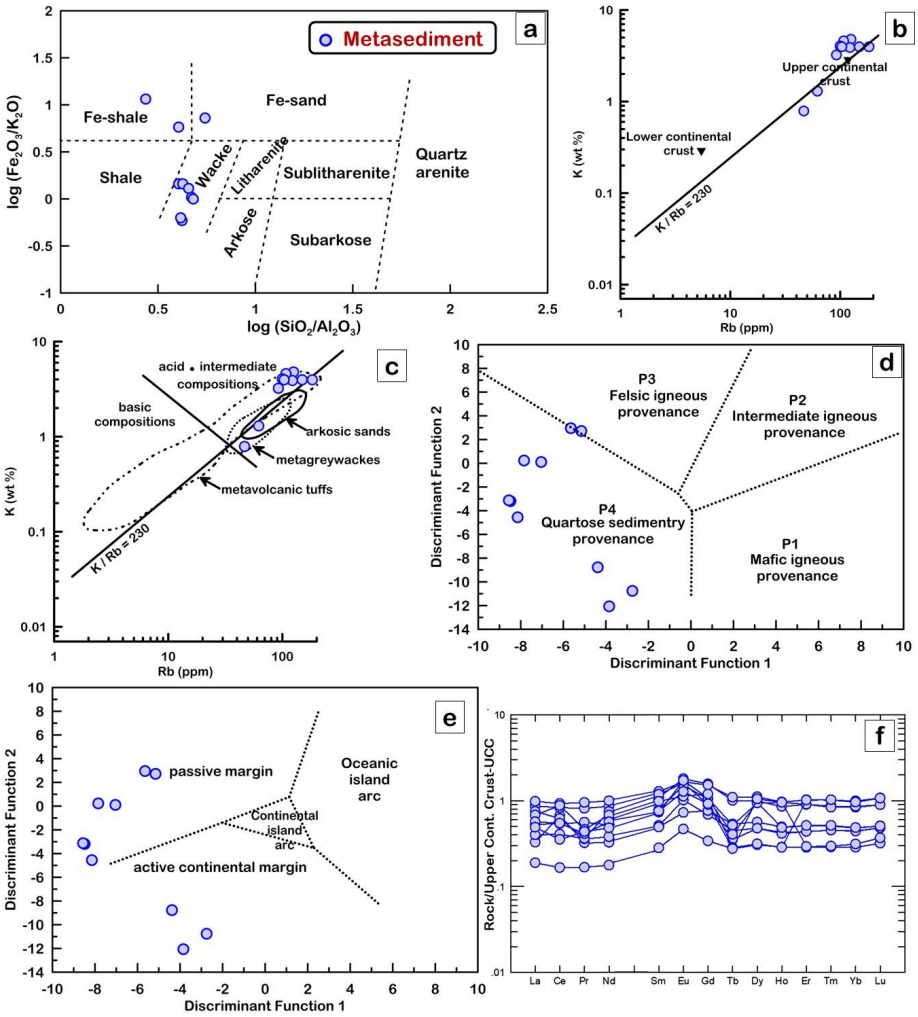

Figure 10. Geochemical classification diagrams of metasediments: (**a**) $\log(Fe_2O_3/K_2O)-\log(SiO_2/Al_2O_3)$ diagram after Herron [36]. (**b**,**c**) K − Rb diagrams after Floyd and Leveridge [38]. Fields of unmetamorphosed arkosic sands after van de Kamp et al. [39], low−grade metagreywackes after Condie et al. [40] and Caby et al. [41], and higher-grade metavolcanic tuffs after van de Kamp [42]; (**d**) plot of samples in discriminant functions F1 vs. F2 (provenance fields are after Roser and Korsch [43]; (**e**) plot of discriminant scores along Function 1 vs. 2 after Bhatia [44]; (**f**) upper continental crust (UCC)−normalized REE patterns [37].

5.2. Alteration Geochemistry

Two main alteration zones surround the Cu-Pb±Zn-bearing ore mineralization in the Halılar area. These are represented by zone-1 (sericite–quartz–chlorite ± kaolinite ± pyrite) and zone-2 (calcite–epidote–albite ± chlorite ± sericite), and they were analyzed for major, trace, and REEs (Table 2). Based on the alteration index (AI) [45] and advanced argillic alteration index (AAAI) of Williams and Davidson [46], samples from each zone show opposite alteration trends (Figure 11a). The ore zone and alteration zone-1 fall along the trend of silicification/potassic alteration, while alteration zone-2 falls along the carbonation/chloritization alteration trend (Figure 11a). Based on the alteration boxplot relationship between the chlorite–carbonate–pyrite index (CCPI) of Large et al. [47] and the AI of Ishikawa et al. [45], the samples of the ore zone and zone-1 are clustered in the field of strongly altered rock, having chlorite–sericite–pyrite alteration while the ore zone is affected by extensive pyritization (Figure 11b). On the other hand, zone-2, within the carbonate-altered host rock field, shows Mn–carbonate–sericite–chlorite alteration (Figure 11b).

Table 2. Major oxides and trace and rare-earth elements (REE) of the ore zone and alteration zones 1 and 2 in the Halılar area.

	Ore Zone			Zone 1 (Sericite-Quartz-Chlorite ± Kaolinite ± Pyrite)															Zone 2 (Calcite-Epidote-Albite ± Chlorite ± Sericite)								
Major Oxides (%)	**H1-a**	**H2**	**H-25**	**H-40**	**H1-b**	**H3-1**	**H3-2**	**H5**	**H-6**	**H-7**	**H-8**	**H-9**	**H-11**	**H-12**	**H-13**	**H-21**	**H-26**	**H-28**		**H4**	**H-10**	**H-16**	**H-17**	**H-19**	**H-23**	**H-27**	**H-30**	**H-41**
SiO_2	39.5	21.3	38.6	15.2	75.7	88.6	91.2	80.2	79.1	71.3	87.0	78.5	66.3	88.2	57.9	83.0	67.4	89.7	SiO_2	61.3	60.4	61.6	54.2	57.3	57.4	63.7	37.8	75.0
Al_2O_3	2.1	3.5	0.8	1.3	4.8	2.3	1.5	6.5	7.0	6.0	4.0	2.3	4.3	4.0	16.6	6.0	9.1	2.8	Al_2O_3	19.2	15.8	13.6	16.5	15.2	15.3	17.9	12.4	12.7
Fe_2O_3	11.7	15.9	14.2	18.6	7.3	2.6	2.5	7.1	3.5	10.5	5.0	6.5	7.3	2.8	9.1	1.8	4.6	2.8	Fe_2O_3	5.2	7.1	6.6	11.9	9.1	7.4	4.7	7.4	0.7
MgO	0.0	0.7	0.3	0.1	1.7	0.6	0.3	1.9	1.1	0.2	1.9	0.1	1.4	1.0	3.3	0.9	1.4	1.2	MgO	1.2	4.9	5.0	4.6	5.9	5.7	2.0	5.5	0.2
CaO	0.0	0.0	0.0	0.0	0.1	0.0	0.0	0.1	0.1	0.0	0.0	0.0	0.0	0.1	0.1	2.8	2.7	0.9	CaO	2.8	0.7	2.8	2.1	0.4	2.8	0.3	19.3	0.8
Na_2O	0.0	0.0	0.0	0.0		0.0	0.0	0.1	0.0	0.0				0.0	0.1	0.1	0.1	0.0	Na_2O	1.9	3.0	2.3	3.4	2.1	2.6	2.1	1.8	3.3
K_2O	0.8	0.8	0.0	0.2	0.5	0.6	0.3	2.0	2.4	3.7	0.1	1.2	0.7	0.8	6.5	2.3	5.0	0.3	K_2O	3.4	3.4	3.1	2.1	4.5	3.1	5.7	2.5	5.0
TiO_2	0.0	0.0	0.0	0.0	0.2	0.0	0.0	0.1	0.2	0.1	0.0	0.1	0.0	0.1	0.6	0.1	0.4	0.0	TiO_2	0.6	0.8	0.8	1.1	0.8	0.8	0.5	0.6	0.0
P_2O_5	0.0	0.0	0.0	0.0	0.0	0.0	0.0	0.1	0.0	0.0	0.0	0.0		0.1	0.1	0.0	0.1		P_2O_5	0.1	0.2	0.2	0.3	0.2	0.2	0.2	0.1	0.0
MnO	0.0	0.0	0.0	0.0	0.1	0.0	0.0	0.1	0.0		0.1		0.1	0.1	0.2	0.1	0.2	0.1	MnO	0.2	0.2	0.2	0.2	0.3	0.2	0.1	0.2	0.0
Cr_2O_3	0.0	0.0	0.0	0.0	0.0			0.0	0.0						0.0	0.0	0.0	0.0	Cr_2O_3	0.0	0.0	0.0	0.0	0.0	0.0	0.0	0.1	0.0
LOI	9.7	14.6	17.1	13.9	4.2	1.7	1.4	1.3	3.1	3.9	1.4	3.9	6.2	1.3	4.5	2.5	3.2	1.1	LOI	4.0	3.2	3.6	3.2	3.4	4.2	2.4	11.8	1.5
Trace and Rare Earth Elements (ppm)																												
Ag	328.7	677.8	34.0	781.3	3.3	18.8	3.3	4.7	6.2	66.2	3.3	112.5	24.1	27.3	9.9	1.3	14.4	2.6	Ag	1.6	11.7	2.9	8.5	11.0	1.6	2.6	0.4	13.6
As	188.9	236.0	8084.9	203.5	203.6	41.9	55.9	95.6	78.9	126.1	145.3	475.8	545.0	23.9	48.3	1377.2	68.1	40.6	As	36.0	14.3	28.8	14.5	41.1	23.9	23.7	36.0	27.8
Au	0.5	0.5	1.0	0.6	0.1	0.1	0.1	0.0	0.1	0.1	0.0	0.0	0.0	0.0	0.0	0.0	0.0	0.0	Au	0.1	0.1	0.0	0.0	0.1	0.0	0.1	0.0	0.1
Ba	161.6	227.2	143.2	101.4	77.9	81.4	93.7	235.6	350.5	796.8	14.7	484.6	118.9	85.8	1422.3	684.6	1181.0	191.2	Ba	303.9	846.4	676.1	451.0	1135.4	621.4	951.5	1145.4	461.1
Be	0.6	0.8	2.6	1.3	0.6	0.4	0.6	0.7	1.3	0.7	0.4	0.4	0.5	0.6	2.0	2.5	0.7	2.3	Be	1.7	3.2	5.1	1.8	2.6	4.6	2.6	1.5	4.3
C	62.2	267.0		308.3	106.8	94.6	36.2	353.6	97.4	805.2	3.4	246.0		107.4	230.5	4018.6	5636.7	1006.9	C	4242.9	917.1	3032.0	1153.2	212.1	3317.8	963.9	26,344.0	793.0
Cd	26.8	38.9	1.5	8.7	0.4	0.7	−0.2	−0.1	0.4	0.5	0.2	0.8	0.9	1.1	0.3	0.8	139.4	0.4	Cd	−0.2	0.8	3.5	0.2	0.2	0.3	0.2	0.8	0.6
Co	24.6	28.4	609.6	18.5	32.3	77.1	45.3	23.7	28.3	20.0	31.1	67.6	131.7	32.2	8.0	60.2	25.1	53.3	Co	25.5	17.4	33.1	21.1	26.5	25.4	12.2	23.0	34.3
Cs	1.2	1.3	0.8	1.1	2.4	1.7	1.1	1.7	3.2	3.0	0.2	1.5	0.7	2.3	5.3	3.3	3.8	2.2	Cs	10.9	4.5	11.5	6.7	5.4	9.6	6.9	8.6	3.7
Cu	678,54.1	126,125.6	10,936.9	194,721.6	133.6	4204.9	2824.8	439.9	948.7	1664.1	545.8	4871.0	24,584.5	1340.1	1610.0	30.9	453.6	1677.1	Cu	1.1	58.4	43.2	20.2	41.3	16.5	28.9	19.2	24.9
Ga	5.9	9.8	8.4	5.7	7.7	4.1	5.5	14.3	11.7	20.2	4.2	14.3	8.9	5.7	46.3	22.2	34.7	12.0	Ga	24.2	37.2	36.6	31.9	48.3	36.9	39.1	48.9	21.0
Hf	0.1	0.3	0.0	0.1	0.2	0.1	0.0	0.2	0.3	0.5	0.1	0.2	0.1	0.1	1.6	0.2	1.3	0.1	Hf	2.6	1.8	1.2	1.0	1.4	0.8	0.4	0.8	2.5
In	0.3	0.3	0.1	0.1	0.2	0.1	0.0	0.0	0.1	0.0	0.0	0.1	0.3	0.0	0.0	0.0	0.2	0.0	In	0.1	0.1	0.1	0.1	0.0	0.0	0.0	0.0	0.0
Ir	0.0	0.1	0.0	0.0	0.0	0.1	0.0	0.0	0.0	0.1	0.0	0.0	0.0	0.0	0.0	0.0	0.0	0.0	Ir	0.0	0.1	0.0	0.0	0.0	0.0	0.0	0.0	0.0
Li	66.2	34.1	28.3	54.0	38.6	39.9	39.0	51.3	64.2	35.1	70.2	41.5	43.0	60.5	64.6	79.9	42.4	65.4	Li	32.8	64.7	73.9	70.0	84.6	76.6	25.5	61.3	29.6
Mo	33.0		15.0	137.0	11.0	24.0	21.0	22.0	69.0	48.0	24.0	84.0	37.0		45.0		4.0	9.0	Mo	5.0	3.0		1.0	6.0	2.0	4.0	2.0	4.0
Ni	8.7	12.2	7.7	7.7	11.4	8.8	19.6	9.7	5.0	2.3	12.8	6.8	32.1	1.6	15.8	17.5	27.1	7.5	Ni	30.7	45.3	70.5	23.8	58.7	32.3	12.9	37.9	8.5
Pb	81,009.8	191,128.0	5958.0	175,698.2	54.4	415.0	90.6	430.8	1427.6	1242.6	372.6	698.9	108.3	7088.1	1459.1	155.5	3864.8	75.8	Pb	9.4	78.2	45.9	28.0	51.1	38.2	43.5	24.9	112.5
Pd	0.1	0.2	0.1	0.1	0.2	0.2	0.1	0.4	0.3	0.8	0.2	0.3	0.1	0.1	2.1	0.2	1.9	0.1	Pd	4.0	2.6	1.1	1.0	1.9	0.6	0.6	0.9	3.0
Pt	0.1	0.1	0.1	0.0	0.0	0.0	0.0	0.0	0.1	0.0	0.0	0.0	0.2	0.1	0.0	0.1	0.0	0.1	Pt	0.0	0.0	0.1	0.0	0.0	0.0	0.1	0.0	0.0
Rb	27.5	33.5	4.7	10.1	17.1	21.7	10.6	47.8	67.4	95.1	1.8	36.1	18.5	24.8	225.5	85.3	169.7	17.3	Rb	110.3	131.7	139.4	85.2	186.5	143.4	148.8	98.2	130.6
Rh	1.9	2.7	0.3	3.4	0.0	0.1	0.1	0.0	0.1	0.1	0.0	0.1	0.5	0.1	0.1	0.0	0.1	0.1	Rh	0.0	0.1	0.1	0.1	0.0	0.1	0.1	0.0	0.0
Ru	0.1	0.1	0.0	0.0	0.0	0.0	0.0	0.0	0.0	0.0	0.0	0.0	0.0	0.0	0.0	0.0	0.1	0.0	Ru	0.0	0.0	0.0	0.0	0.0	0.0	0.0	0.0	0.0
S	162,930.0	211,150.0	256,310.0	203,370.0	34,415.0	11,038.0	6804.3	824.7	15,500.0	24,925.0	580.8	35,579.0	59,632.0	3205.2	759.1	1139.3	4052.6	3609.0	S	529.9	327.8	392.5	482.6	3094.1	1553.3	497.5	2868.3	2847.1
Sb	23.2	15.5	12.5	27.7	4.5	6.7	5.4	7.8	6.2	12.5	5.4	13.0	8.0	5.6	5.1	21.2	5.3	5.4	Sb	2.1	2.0	1.4	2.7	4.1	1.0	2.3	1.8	3.2
Sn	0.5	0.8	0.6	0.5	1.9	0.6	0.9	1.0	1.1	0.9	0.4	1.2	0.6	1.0	2.9	1.0	1.7	0.5	Sn	2.4	3.3	2.3	2.8	7.2	2.3	7.5	1.6	0.6
Sr	14.7	85.1	224.1	89.1	5.7	6.8	8.1	16.5	21.6	35.7	2.8	15.9	7.9	7.3	86.1	214.7	85.7	238.4	Sr	127.7	232.5	408.8	320.7	197.7	329.9	114.8	289.8	274.6
Te	16.9	35.8	2.5	27.9	0.5	0.9	0.3	0.7	0.9	4.7	0.4	2.8	1.1	1.4	0.4	0.1	0.1	0.0	Te	0.0	0.1	0.0	0.0	0.1	0.0	0.0	0.0	0.1
Tl	1.5	2.8	0.1	2.3	0.2	0.4	0.2	0.7	1.1	1.6	0.0	0.7	0.2	0.3	2.8	1.2	2.2	0.2	Tl	1.3	1.4	1.3	0.8	2.1	1.3	1.3	1.2	1.3
Zn	4328.1	5932.9	356.5	1038.0	63.3	20.9	35.5	64.9	32.6	89.8	116.6	37.3	88.7	141.9	69.7	211.4	25,117.3	270.7	Zn	57.7	134.2	122.0	74.9	102.4	97.4	3.2	65.3	225.6
Se	192.8	377.5	54.4	472.5	3.4	5.0	6.5	6.8	4.4	19.8	6.7	29.9	7.7	4.7	2.9	6.0	3.1	2.1	Se	1.7	4.1	1.5	0.8	3.6	7.7	−1.1	2.8	4.3
Sc	53.4	31.5	54.4	31.0	141.8	176.2	146.9	111.3	157.7	167.0	141.9	172.2	137.9	157.7	178.7	118.7	149.7	135.3	Sc	126.6	163.1	120.7	125.2	119.5	147.6	143.5	100.8	159.6

Table 2. *Cont.*

	Ore Zone	Zone 1 (Sericite-Quartz-Chlorite ± Kaolinite ± Pyrite)																	Zone 2 (Calcite-Epidote-Albite ± Chlorite ± Sericite)								
Major Oxides (%)	**H1-a**	**H2**	**H-25**	**H-40**	**H1-b**	**H3-1**	**H3-2**	**H5**	**H-6**	**H-7**	**H-8**	**H-9**	**H-11**	**H-12**	**H-13**	**H-21**	**H-26**	**H-28**		**H4**	**H-10**	**H-16**	**H-17**	**H-19**	**H-23**	**H-27**	**H-30**	**H-41**
Y	0.2	1.2	0.4	0.4	2.5	0.6	0.4	1.3	2.5	2.9	1.2	1.0	1.5	1.4	13.7	4.3	12.1	1.2	Y	15.3	15.7	16.6	14.3	10.8	22.2	13.0	9.5	10.7
La	0.5	2.3	0.2	1.3	6.7	1.4	0.5	1.3	5.0	3.9	0.9	1.9	0.5	1.3	21.9	6.3	11.3	0.9	La	40.5	17.4	26.3	16.7	15.3	35.0	21.6	10.1	22.5
Ce	1.0	3.7	0.4	2.3	13.3	2.7	0.9	1.8	7.2	7.9	1.8	3.5	0.7	2.0	42.6	11.5	22.4	1.7	Ce	73.9	30.0	51.2	36.7	40.8	70.2	32.7	19.9	46.9
Pr	0.1	0.4	0.1	0.3	1.5	0.3	0.1	0.3	0.9	0.9	0.2	0.4	0.1	0.3	5.1	1.3	2.6	0.2	Pr	7.8	4.5	6.1	4.2	3.7	8.1	5.0	2.3	4.9
Nd	0.3	1.3	0.2	1.0	5.4	1.1	0.4	1.1	3.2	3.2	0.9	1.4	0.4	1.3	19.5	5.0	10.2	0.9	Nd	27.5	17.1	23.4	16.8	14.3	30.9	18.2	8.9	16.7
Sm	0.2	0.4	0.1	0.2	1.1	0.3	0.1	0.4	0.8	1.4	0.2	0.7	0.2	0.4	5.3	1.3	2.9	0.2	Sm	4.8	4.4	5.0	3.8	3.6	6.5	4.1	2.8	3.2
Eu	0.1	0.1	0.0	0.0	0.3	0.1	0.1	0.2	0.3	0.7	0.1	0.3	0.1	0.1	1.7	0.4	0.9	0.1	Eu	1.0	1.3	1.2	1.5	0.9	1.6	1.2	1.2	0.5
Gd	0.1	0.4	0.1	0.2	1.2	0.3	0.1	0.3	0.7	0.9	0.2	0.4	0.2	0.4	4.8	1.2	2.9	0.2	Gd	6.0	4.7	5.3	4.6	4.0	6.9	3.6	2.4	3.8
Tb	0.0	0.0	0.0	0.0	0.1	0.0	0.0	0.0	0.1	0.1	0.0	0.0	0.0	0.1	0.5	0.1	0.4	0.0	Tb	0.6	0.6	0.6	0.5	0.4	0.8	0.5	0.3	0.3
Dy	0.0	0.3	0.1	0.1	0.6	0.1	0.1	0.3	0.5	0.6	0.2	0.2	0.3	0.3	2.9	0.8	2.1	0.2	Dy	2.9	3.3	3.6	2.9	2.3	4.6	2.8	2.0	1.8
Ho	0.0	0.1	0.0	0.0	0.1	0.0	0.0	0.1	0.1	0.1	0.1	0.1	0.1	0.1	0.6	0.2	0.4	0.1	Ho	0.5	0.6	0.7	0.6	0.5	0.9	0.5	0.4	0.4
Er	0.0	0.2	0.0	0.1	0.3	0.1	0.1	0.2	0.3	0.4	0.1	0.1	0.2	0.2	1.7	0.5	1.3	0.1	Er	1.7	1.9	2.0	1.6	1.3	2.7	1.7	1.2	1.3
Tm	0.0	0.0	0.0	0.0	0.0	0.0	0.0	0.0	0.0	0.1	0.0	0.0	0.0	0.0	0.2	0.1	0.2	0.0	Tm	0.3	0.3	0.3	0.2	0.2	0.4	0.2	0.2	0.2
Yb	0.0	0.1	0.0	0.0	0.3	0.1	0.0	0.2	0.3	0.4	0.1	0.1	0.1	0.2	1.5	0.5	1.2	0.1	Yb	1.8	1.6	1.7	1.3	1.2	2.4	1.6	1.1	1.6
Lu	0.0	0.0	0.0	0.0	0.0	0.0	0.0	0.0	0.0	0.1	0.0	0.0	0.0	0.0	0.3	0.1	0.2	0.0	Lu	0.3	0.3	0.3	0.2	0.2	0.4	0.2	0.2	0.3
Th	0.3	1.7	0.2	0.4	2.4	1.0	0.2	0.9	1.5	2.6	0.5	1.1	0.2	0.6	8.9	1.8	5.7	0.3	Th	14.6	10.5	9.7	6.4	9.8	13.8	12.1	7.4	16.3
Parameters																			*Parameters*									
CCPI	93.2	94.6	99.7	99.0	94.1	82.0	88.1	79.7	63.5	71.8	97.9	83.4	91.8	80.2	63.4	51.6	51.7	92.3	CCPI	53.0	63.8	66.6	73.5	68.3	68.4	44.5	73.7	8.9
Ishikawa AI	98.8	99.0	95.2	96.2	97.3	95.6	93.0	94.6	97.5	98.1	98.2	97.9	98.0	95.5	98.2	53.3	68.7	61.9	Ishikawa AI	50.0	69.7	61.3	55.0	80.3	61.9	76.0	27.5	55.8
AAAI	98.6	76.0	92.5	93.1	81.0	92.9	95.9	79.2	86.7	96.7	82.0	98.8	82.4	89.1	62.7	68.7	61.4	80.7	AAAI	51.2	41.4	38.0	34.8	40.3	33.9	59.1	12.4	63.7

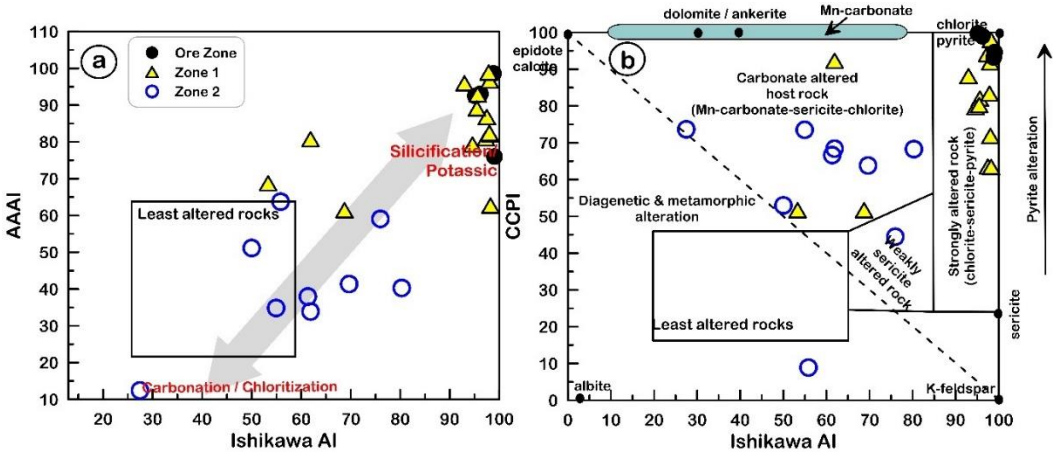

Figure 11. (**a**) AI [45] vs. AAAI [46]; (**b**) AI [45] vs. CCPI [47] of the studied alteration samples from the Halılar area.

5.3. Mass Balance Calculations

The behavior of different elements, excluding immobile ones, is changeable during hydrothermal alteration processes depending on their volume changes and their mass transfer [48,49]. Gresens [33] and Grant [34,35] used mass-balance calculations to quantify hydrothermal alteration effects on the host rock within the mineralized regions and to determine the relative gain and loss of the various major and trace elements during hydrothermal alteration.

Based on the trace element geochemical analyses, the ore zone and alteration zone-1 have high amounts of Cu and Pb, with an average of 9.9% and 11.3%, respectively, for the ore zone, and 0.32% and 0.12%, respectively, for zone-1 (Table 2). They are classified as a Cu-Pb type (Figure 12), which refers to the high concentrations of chalcopyrite and galena. Alteration zone-2 represents the Cu-Pb-Zn type (Figure 12), having low Cu, Pb, and Zn contents, with averages of 28.18ppm, 47.95ppm, and 98.07ppm, respectively.

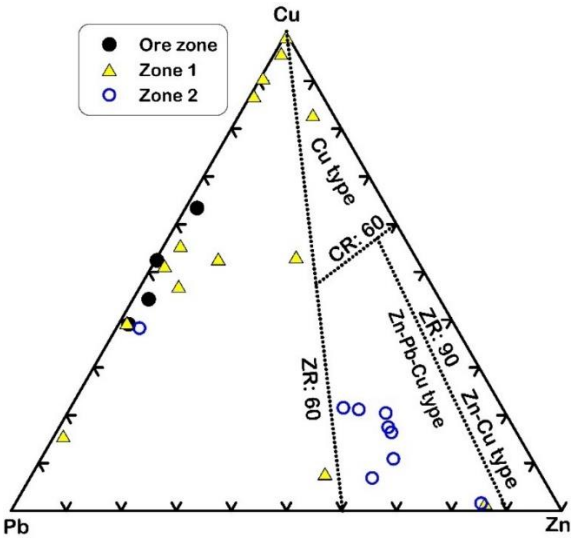

Figure 12. Metal content classification diagram after Large [50]. The ratios ZR = (100 Zn/(Zn + Pb) and CR = 100 Cu/(Cu + Zn) are based on the average ore grades in mass percent after Large [50].

Al_2O_3 and TiO_2 are immobile in all alteration zones during hydrothermal alteration; therefore, they were selected to assess the chemical changes due to the process of hydrothermal alteration by using the GEOISO-Windows software developed by Coelho [32]. The results of these calculations are illustrated through the isocon diagrams of Grant [34] and

show the different patterns of major and trace element gains and losses (Figures 13 and 14 and Table 3). The samples from zone-1 are rich in SiO_2, Fe_2O_3, K_2O, and LOI, with lesser increases in the amount of CaO, P_2O_5, and MnO (Figure 14a). Gains in Ag, As, Cu, Mo, Pb, S, Sb, and Zn are also recognized within this alteration zone (Figure 14b). This zone is characterized by higher amounts of sulfur and iron, with variable copper, lead, and zinc contents reflecting high pyritization, with the main base metals providing higher mass (MC = 170.42) and volume change (VC = 182.1) (Table 3). SiO_2 and K_2O increases reflect high silicification and sericitization, which are comparable with the petrographic and mineralogical (XRD) data. In zone-2, CaO, Na_2O, P_2O_5, TiO_2, LOI, and carbon are enriched, reflecting calcite, epidote, and albite alterations (Figure 14c). The loss of Cu, Pb, and Zn is observed in this zone, providing lower MC (−3.18) and VC (−1.80) values (Figure 14d and Table 3).

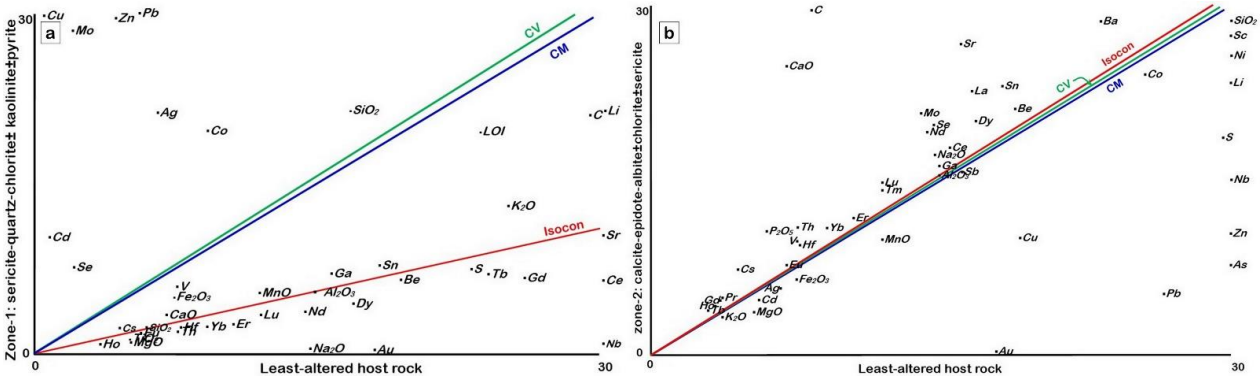

Figure 13. Isocon diagram comparing the mean composition of least-altered samples and altered samples from (**a**) alteration zone-1 (sericite–quartz–chlorite ± kaolinite ± pyrite) and (**b**) alteration zone-2 (calcite–epidote–albite ± chlorite ± sericite).

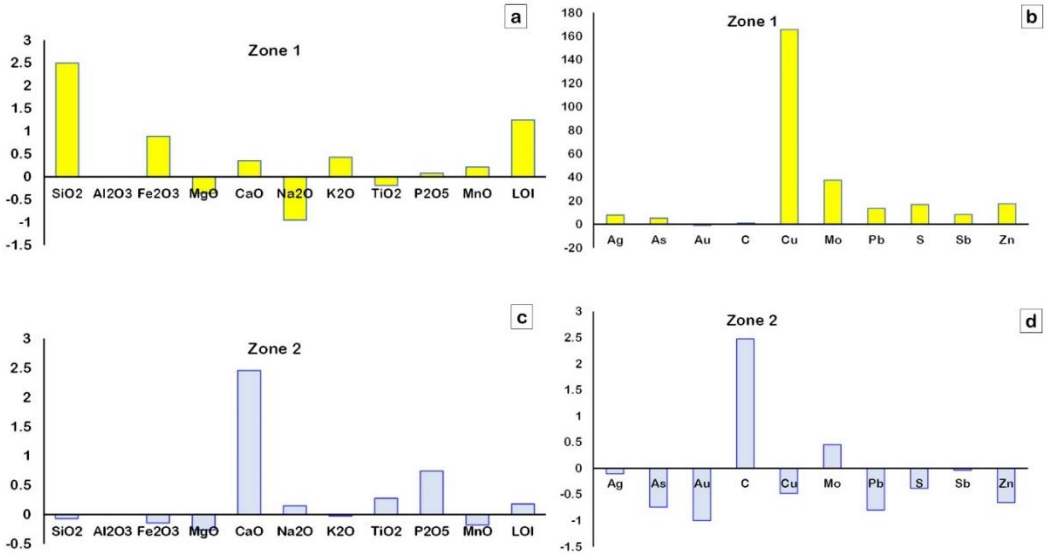

Figure 14. Gain/loss of major oxides (wt. %) (**a**,**c**) and trace elements (ppm) (**b**,**d**) in the alteration zones during hydrothermal alteration based on the mean data of the representative least−altered samples as a reference for calculations.

Table 3. Element/oxide mass changes in relation to the original whole-rock mass ((Mfi-Moi)/Mo) and in relation to the original element/oxide mass in the original rock ((Mfi-Moi)/Moi).

	Zone 1		**Zone 2**	
	(Mfi-Moi)/Mo	**(Mfi-Moi)/Moi**	**(Mfi-Moi)/Mo**	**(Mfi-Moi)/Moi**
SiO_2	152.3	2.5	−4.1	−0.1
Al_2O_3	0.0	0.0	0.0	0.0
Fe_2O_3	6.7	0.9	−1.1	−0.1
MgO	−1.8	−0.4	−1.3	−0.3
CaO	0.4	0.4	2.5	2.5
Na_2O	−2.0	−0.9	0.3	0.1
K_2O	1.5	0.4	−0.1	0.0
TiO_2	−0.1	−0.2	0.1	0.3
P_2O_5	0.0	0.1	0.1	0.7
MnO	0.0	0.2	0.0	−0.2
LOI	4.3	1.3	0.6	0.2
Ag	51.0	7.8	−0.7	−0.1
As	538.8	5.2	−77.2	−0.7
Au	−44.3	−1.0	−44.4	−1.0
Ba	532.3	0.9	117.4	0.2
Be	−0.1	0.0	0.2	0.1
C	1192.7	0.9	3139.3	2.5
Cd	27.3	34.2	−0.1	−0.2
Co	97.2	3.8	−2.1	−0.1
Cs	1.7	0.4	2.8	0.6
Cu	8702.9	165.5	−25.3	−0.5
Ga	8.1	0.2	2.1	0.1
Hf	−0.2	−0.1	0.2	0.2
Li	68.6	0.9	−17.7	−0.2
Mo	74.9	37.4	0.9	0.5
Nb	−186.5	−0.9	−101.0	−0.5
Ni	−6.9	−0.2	−6.8	−0.2
Pb	3144.6	13.5	−186.1	−0.8
S	36,833.0	16.8	−842.1	−0.4
Sb	19.3	8.4	−0.1	0.0
Se	18.9	9.0	0.6	0.3
Sn	0.4	0.2	0.6	0.2
Sr	−7.1	0.0	94.4	0.6
V	8.9	1.2	2.1	0.3
Zn	4815.7	17.4	−181.1	−0.7
Zr	−15.5	−0.2	76.2	0.8
Sc	258.7	1.8	−15.8	−0.1
Y	−2.8	−0.2	2.0	0.2
La	−4.3	−0.3	5.5	0.3
Ce	−15.3	−0.4	4.8	0.1
Pr	−0.9	−0.3	1.3	0.3
Nd	−3.9	−0.3	4.4	0.3
Sm	−0.4	−0.1	0.8	0.2
Eu	0.0	0.0	0.1	0.1
Gd	−1.1	−0.3	0.7	0.2
Tb	−0.1	−0.2	0.1	0.3
Dy	−0.6	−0.3	0.4	0.2
Ho	−0.1	−0.2	0.1	0.1
Er	−0.4	−0.3	0.2	0.1
Tm	0.0	−0.2	0.0	0.2
Yb	−0.3	−0.2	0.2	0.2
Lu	0.0	−0.2	0.0	0.2
Th	−2.2	−0.3	3.2	0.4
Mass change	**MC= 170.4**		**MC = -3.2**	
Volume change	**VC = 182.1**		**VC = -1.8**	

6. Sulfur Isotope ($\delta^{34}S$)

$\delta^{34}S$ isotopic data from the sulfide-bearing ore deposits were obtained to determine the source of the sulfur and the origin of the sulfur-bearing fluids [51]. The $\delta^{34}S$ isotope values of ten pyrite, chalcopyrite, and galena samples collected from the highly altered and mineralized altered metasediments host rocks are in the range of −1.1 to −0.1‰ V_{CDT} (n = 3), −2.7 to −0.5 ‰ V_{CDT} (n = 3), and −3.5 to −2.1‰ V_{CDT} (n = 4), respectively (Table 4). Pyrites from a quartz vein have an average $\delta^{34}S$ of 0.4‰VCDT (Table 4 and Figure 15a). By assuming the H_2S as the sulfur species in solution, and based on the fractionation equations of Czamanske and Rye [52] and Ohmoto and Rye [51], the $\delta^{34}S_{H2S}$ values of the fluid have a narrow range of −2.54 to −0.08 ‰ V_{CDT} (Table 4 and Figure 15b).

Table 4. Sulfur isotope values of sulfides from the Halılar area.

Sample ID	Mineral	Host	Measured $\delta^{34}S$ (‰)	at T°C (1)	$\delta^{34}S_{H2S}$ Fluid (‰) (2)	Error range
H25	pyrite	Mineralized altered rock	−0.1	285.86	−1.4	± 0.3
H2	pyrite	Qz-veined altered rock	−1.1	285.86	−0.9	± 0.3
H1-a	pyrite	Qz-veined altered rock	−0.7	285.86	−2.0	± 0.3
H11	pyrite	Qz-vein	0.4	285.86	−0.9	± 0.3
H25	chalcopyrite	Mineralized altered rock	−0.5	285.86	−0.3	± 0.3
H2	chalcopyrite	Qz-veined altered rock	−2.7	285.86	−2.5	± 0.3
H40	chalcopyrite	Mineralized altered rock	−1.1	285.86	−0.9	± 0.3
H1-a	galena	Qz-veined altered rock	−3	285.86	−1.0	± 0.2
H2	galena	Qz-veined altered rock	−3.4	285.86	−1.4	± 0.2
H25	galena	Mineralized altered rock	−2.1	285.86	−0.1	± 0.2
H40	galena	Mineralized altered rock	−3.5	285.86	−1.5	± 0.2

(1) Based on the fluid inclusion thermometry (unpublished data), (2) Calculated by using the sulfur isotope fractionation equations in Czamanske and Rye [52] and Ohmoto and Rye [51].

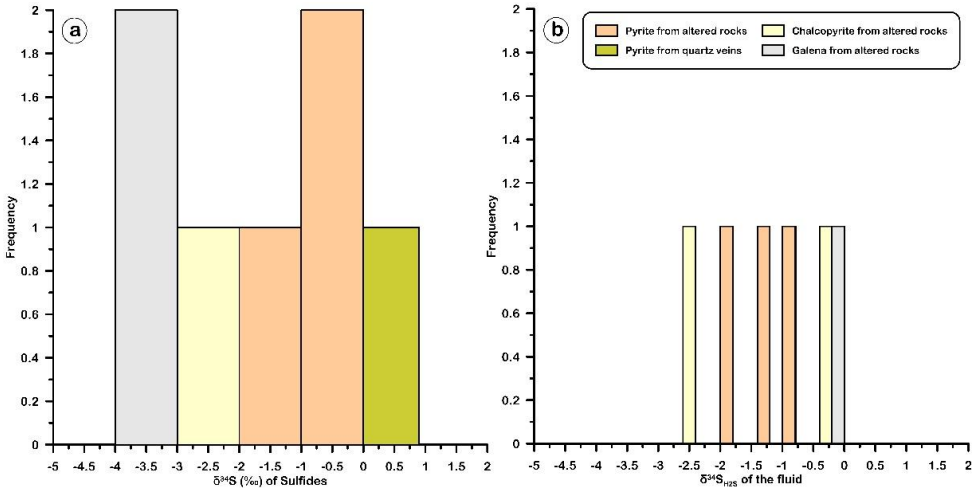

Figure 15. Histograms of (**a**) the $\delta^{34}S$ isotopic compositions for sulfide minerals (pyrite, chalcopyrite, and galena) and (**b**) the $\delta^{34}S_{H2S}$ of the fluid that formed the sulfides in the Halılar area.

7. Discussion

7.1. Sources of Sulfur

There are many sulfur sources with distinct $\delta^{34}S$ values: (1) the mantle source has a 0 ± 3‰ $\delta^{34}S$ value [53]; (2) the magmatic source, in which the sulfur resulted from desulfidation and/or dissolution or from magmatic sulfides, has 0 to +9‰ $\delta^{34}S$ [54]; (3) the seawater sources have a mean value of +20 ‰ $\delta^{34}S$; and (4) the strongly reduced sulfur source in the sedimentary rocks has very negative $\delta^{34}S$ values [55].

In the Halılar area, the mean $\delta^{34}S$ value of the sulfides is close to −1.62‰, suggesting a uniform magmatic sulfur source in which the sulfur originates either from the leaching and remobilization of the old magmatic sulfide or from the mantle source (Figure 16). Furthermore, the $\delta^{34}S$ values of the studied sulfide minerals decrease from pyrite (−1.1 to 0.4 $‰V_{CDT}$) and chalcopyrite (−2.7 to −0.5 $‰V_{CDT}$) to galena (−3.5 to −2.1$‰V_{CDT}$) (Figure 17), which is compatible with the suggested trend of differentiation of Ohmoto and Rye [51]. Thus, the ore-bearing fluid appears to have a magmatic (mantle) source [51] with magmatic–hydrothermal signatures [56] (Figure 18).

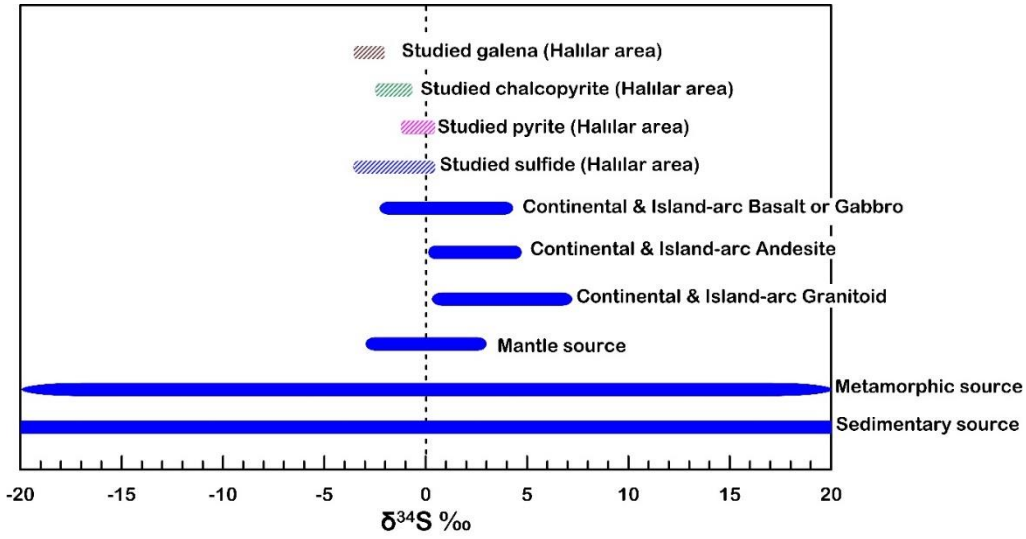

Figure 16. $\delta^{34}S$ values of sulfides from the mantle, the continental igneous setting, and metamorphic and sedimentary sources. Mantle source [53], island arc basalts and gabbros [57,58], andesites [59,60], granitoids [61–63], and metamorphic and sedimentary sources [64].

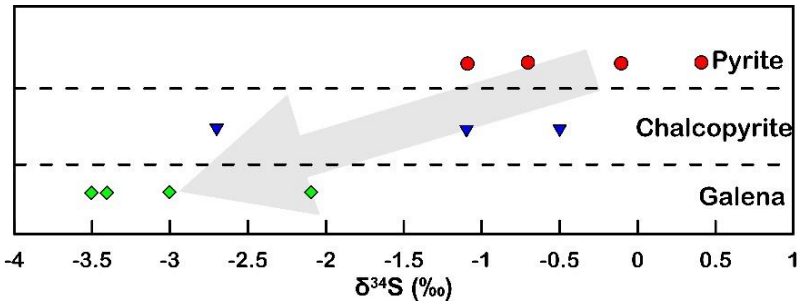

Figure 17. Distribution of the $\delta^{34}S$ values in the studied sulfide minerals from the Halılar area.

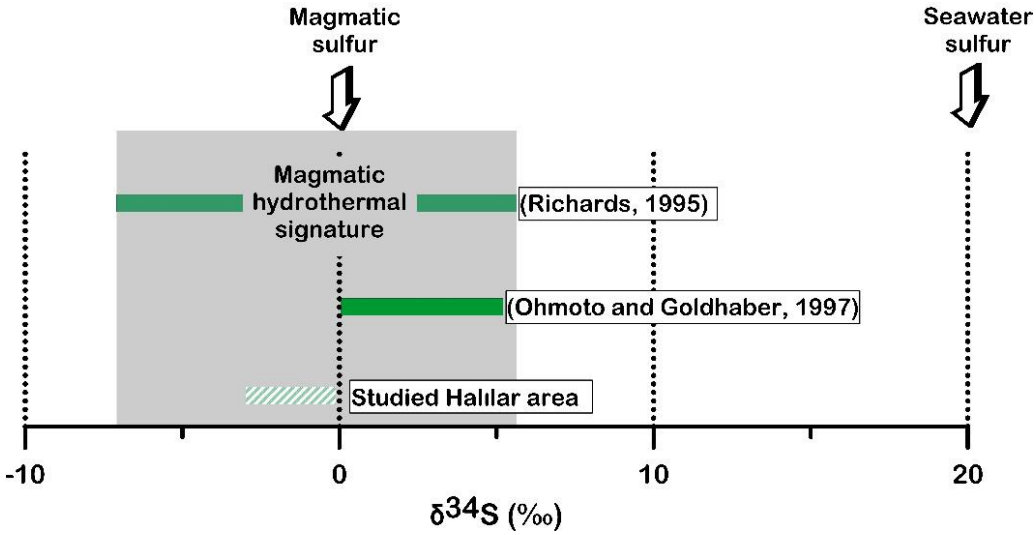

Figure 18. $\delta^{34}S$ values from the Halılar area compared with the magmatic−hydrothermal deposits [51,56].

7.2. Metal Source

The metasediments of the Sakarkaya Formation that host the Halılar Cu-Pb (±Zn) mineralization are slightly enriched in metallic elements (average of Ag = 6.7 ppm, As = 101.9 ppm, Au = 0.04 ppm, Cu = 53.8 ppm, Mo = 1.8 ppm, Pb = 274.7 ppm, S = 389.0 ppm, Sb = 2.0 ppm, and Zn = 371.3 ppm) relative to the average UCC (Table 5). Moreover, the contents of the metallic elements in the Düztarla granitoid rocks also show higher values than typical UCC (mean values of Ag = 1.14 ppm, As = 84.05 ppm, Au = 0.36 ppm, Cu = 368.91 ppm, Mo = 324.68 ppm, Pb = 49.52 ppm, S = 1396.7 ppm, Sb = 2.34 ppm, and Zn = 414.69 ppm).

Table 5. Upper continental crust (UCC)–normalized elements of metasediments in Sakarkaya Formation and Düztarla granitoid rocks.

		Ag	As	Au	Cu	Mo	Pb	S	Sb	Zn
UCC		50 *	1.5 *	1.8 *	25 *	1.5 *	17 *	621 **	0.2 *	71 *
Metasediments normalized to UCC (ppm)	H-14	0.0	22.3	0.0	0.7	0.7	2.0	0.6	9.8	2.8
	H-15	0.2	16.4	0.0	2.6	1.3	6.0	0.3	6.4	1.0
	H-18	0.2	9.9	0.0	0.8	0.0	3.2	0.2	5.4	3.8
	H-20	0.0	14.0	0.0	1.4	0.0	3.6	1.5	10.7	3.6
	H-22a	0.1	282.9	0.0	5.0	2.0	53.6	1.4	26.3	8.2
	H05	0.1	13.2	0.0	1.6	1.7	13.7	0.4	7.6	5.9
	H07	0.2	12.0	0.0	1.7	1.7	16.0	0.3	8.6	7.1
	H09	0.1	148.4	0.0	1.1	1.7	18.0	0.9	8.1	6.5
	H55	0.1	148.0	0.0	3.2	1.8	21.0	0.4	9.2	6.8
	H60	0.1	12.6	0.0	3.3	1.8	24.5	0.3	8.1	6.6
Granitoid normalized to UCC		0.0	56.0	0.2	14.8	216.5	2.9	2.2	11.7	5.8

* UCC after Taylor and McLennan [37]; ** UCC after Rudnick et al. [65].

When the sulfur is normalized to the UCC of Rudnick et al. [65], it is highly rich in granitoid rocks, but not in metasediments (Figure 19a,b). Thus, the primary metal suppliers appear to be the metasediments and intrusive Düztarla granitoid magmatism; together, they account for the metals in the Halılar brecciated-stockwork-type mineralization. Based on the geologic features and mode of occurrences, the Halılar metasediment-hosted Cu-Pb (±Zn) mineralization appears to be formed by epigenetic hydrothermal processes after sedimentation/diagenesis and metamorphism.

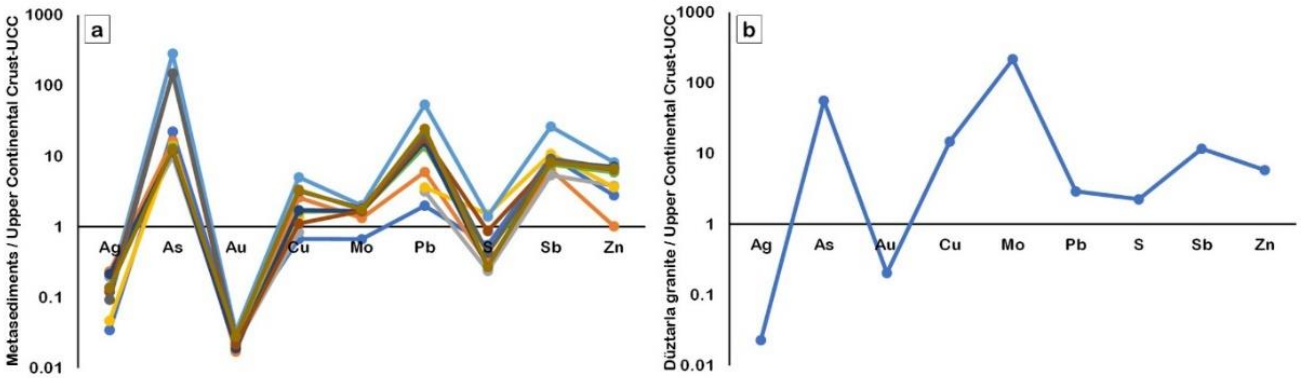

Figure 19. Upper continental crust (UCC)–normalized elements diagram of the metasediments (**a**) and Düztarla granitoid (**b**). After Taylor and McLennan [37] and Rudnick et al. [65].

8. Conclusions

The Halılar area contains two groups: the clastic Halılar Group that overlies the metamorphics of the pre-Late Triassic age or Permian limestones and the Bilecik Group. The Halılar Group consists of the Bağcağız and Sakarkaya Formations, and the Bilecik Group is represented by two formations, including the Taşçıbayırı Formation and the Günören Limestone. The Sakarkaya and Bağcağız Formations were later intruded by Oligo–Miocene Düztarla granitoid rocks.

The Halılar base metal mineralization consists mainly of Cu-Pb sulfide with some Zn sulfide in the brecciated stockworks and veins. This type of vein mineralization is restricted to a fault gouge zone directed NE–SW and along the lower contact of the Sakarkaya and Düztarla granitic rocks. Two types of hydrothermal alteration zones with gradual boundaries can be observed in the main ore zone. These include zone-1 (sericite–quartz–chlorite ± kaolinite ± pyrite) and zone-2 (calcite–epidote–albite ± chlorite ± sericite). The main ore mineral assemblage consists of chalcopyrite, galena, pyrite, and sphalerite in an abundant amount of gangue minerals such as quartz, sericite, chlorite, and calcite forming along the quartz stockwork veins, as well as in the brecciated ore zones. The other oxidation and supergene mineralization includes covellite and goethite formed after chalcopyrite and pyrite, respectively.

The least-altered Sakarkaya metasediments are classified mainly as wackes and, rarely, Fe-sand and Fe-shale, which are relatively similar in chemical composition to the upper continental crust (UCC). They are sourced from the crustal felsic rocks and a quartzose sedimentary provenance formed within the passive and active continental margins. Mass-balance calculations reveal that the samples of zone-1 are enriched in SiO_2, Fe_2O_3, K_2O, and LOI, with Ag, As, Cu, Mo, Pb, S, Sb, and Zn reflecting a high degree of pyritization with sericitization and silicification. On the other hand, the samples of zone-2 show an increase in CaO; Na_2O; P_2O_5; TiO_2; LOI; and carbon-reflecting calcite, epidote, and albite alterations.

The mean $\delta^{34}S$ value of the sulfides in the Halılar area is close to −1.62‰, suggesting a uniform magmatic sulfur source in which the sulfur originates either from leaching and remobilization from the old magmatic sulfide or from the mantle source. There is also a sulfur isotope having a differentiation trend from pyrite to galena. The ore-bearing fluid has $\delta^{34}S$ values of H_2S, ranging from −2.54 to −0.08 ‰, typical of a magmatic–hydrothermal signature [47].

Based on the normalization of the metallic elements in the Sakarkaya metasediments and Düztarla granitoid rocks to the UCC [38] and [65], these metasediments and granitoid rocks represent the primary source of metals forming the Halılar brecciated-stockwork-veining-type mineralization. Overall, the geologic features and the mode of occurrences of the Halılar metasediment-hosted Cu-Pb (±Zn) mineralization suggest that they were formed by epigenetic hydrothermal processes after sedimentation/diagenesis and metamorphism.

Funding: This work was supported by the BAP Project (No. 37872) of Istanbul Technical University (ITU, Turkey).

Data Availability Statement: The data presented in this study are available in this article and its Appendices A–C.

Acknowledgments: The author would like to acknowledge the assistance of members of the Geochemistry Research Laboratories at Istanbul Technical University (Turkey). Great appreciation goes to M. Kumral (ITU, Turkey) and A. Abdelnasser (Benha University) for their support during all stages of work on the article. Z. Doner (ITU, Turkey) and A. Unal (ITU, Turkey) are also thanked for their help during fieldwork. The help of F. Yavuz (ITU, Turkey) and G. Ustunisik (South Dakota School of Mines, USA) were highly appreciated during the review of the article. The editor and two anonymous reviewers are thanked for carefully reading the manuscript and for their constructive comments.

Conflicts of Interest: The author declares no conflict of interest.

Appendix A

Table A1. XRD analyses of representative samples from the ore zone.

No.	Ref. Code	Compound Name	Chemical Formula	SemiQuant [%]				Average
				H1a	H2	H40	H25	
1	98-005-7052	Quartz low	O2 Si1	35	16	13	51	28.75
2	98-004-6240	Wollastonite 1A, manganoan	Ca2.88 Mn0.12 O9 Si3	8	11	25	19	15.75
3	98-001-7142	Kaolinite 1A	H4 Al2 O9 Si2	10	13	16		9.75
4	98-004-5719	Microcline	Al1 K1 O8 Si3	18	9	1		7.00
5	98-000-5164	Chalcopyrite	Cu1 Fe1 S2	6	6	13	1	6.50
6	98-000-5343	Calcite	C1 Ca1 O3	3	17	5		6.25
7	98-002-8161	Andradite	Ca3 Fe2 O12 Si3	5	5	7		4.25
8	98-004-5343	Anglesite	O4 Pb1 S1	4	4	5	3	4.00
9	98-000-5961	Pyrite	Fe1 S2	4	4	2	6	4.00
10	98-002-1539	Cubanite high	Cu0.3333 Fe0.6667 S1	1	4	7		3.00
11	98-004-9157	Sphalerite ferrous	Fe0.215 S1 Zn0.785	1	2	1	4	2.00
12	98-008-5367	Albite	Al1 Na1 O8 Si3	1	5	1		1.75
13	98-007-8263	Biotite 1M	H1.47 Al1.92 F1.98 Fe2.59 K2 Mg3.15 Mn0.09 O21.47 Si5.98 Ti0.27				6	1.50
14	98-007-9292	Galena	Pb1 S1	1	1	2	1	1.25
15	98-004-9486	Quartz high	O2 Si1	2	1	1		1.00
16	98-002-2578	Halite	Br0.8947 Cl0.1053 Na1	1	2	1		1.00
17	98-001-7351	Goethite	H1 Fe1 O2				4	1.00
18	98-006-2562	Chalcocite high	Cu2 S1				3	0.75
19	98-005-2707	Clinochlore IIb-2	H2 Al2 Mg5 O15 Si3				2	0.50
20	98-002-1503	Barite high	Ba1 O4 S1				1	0.25

Appendix B

Table A2. XRD analyses of representative samples from alteration zone-1 (sericite–quartz–chlorite ± kaolinite ± pyrite).

No.	Ref. Code	Compound Name	Chemical Formula	SemiQuant [%]															Average
				H1b	H3.1	H3.2	H5	H6	H7	H8	H9	H11	H12	H13	H21	H26	H28	H31	H33	
1	98-002-8439	Quartz low	O2 Si1	48	66	83	51	49	56	53	84	64	65	15	58	38	84	63	46	57.69
2	98-001-1941	Muscovite 2M1	H2 Al3 K1 O12 Si3				40	25		32		12	4	2	10	31			25	11.31
3	98-001-2798	Kaolinite 1A	H4 Al2 O9 Si2	9	18	4		15	15	4	4	4	14		4				7	6.13
4	98-001-7363	Microcline	Al1 K1 O8 Si3		6	5	2	6			6	5	4	17	7	10	6		5	4.94
5	98-000-5322	Clinochlore 1MIa	H8 Al3.3 Fe1.65 Mg2.5 O18 Si2.2 H2 Al2.75 Ca0.011 Fe0.032	4	4	2	2			5		4	4	4	4	5	3	14	14	4.31
6	98-005-2472	Sericite 2M1	K0.727 Mg0.022 Na0.17 O12 Si3.128 Ti0.02	36										22	10	1				4.31
7	98-001-7679	Orthoclase	Al1 K0.94 Na0.06 O8 Si3				4		14				3	16		1				2.38
8	98-003-7636	Chamosite 1MIIb	H16 Al5.024 Fe4.964 Mg5.036 O36 Si5.7							4			4	7		5	4	7		1.94
9	98-003-4846	Albite	Al1 Ge2 Na1 O8 Si1			1		3		1				8	3	1				1.06
10	98-002-3975	Calcite	C1 Ca1 O3			2			1		2	6		1	2	1	1			1.00
11	98-002-3340	Pyrite	Fe1 S2	1	1	1		1	2		1	2	1	1	1	1		1	1	0.94
12	98-007-8271	Biotite 1M	H1.47 Al1.92 F1.98 Fe2.59 K2 Mg3.15 Mn0.09 O21.47 Si5.98 Ti0.27						7					3		1		4		0.94
13	98-000-5164	Chalcopyrite	Cu1 Fe1 S2		1							2	1	1	1	1				0.44
14	98-006-1164	Andradite	Ca3 Fe2 O12 Si3															6		0.38
15	98-008-5911	Dolomite	C2 Ca1 Mg1 O6						2		1			1		2				0.38
16	98-004-5305	Chalcophyllite	H48 Al1 As2 Cu9 O44 S1.5	2													1	1	1	0.31
17	98-004-1521	Magnetite	Fe3 O4					1	1					1		1		1		0.31
18	98-005-1007	Sphalerite	Fe0.372 S1 Zn0.628						1		1							1	1	0.25
19	98-001-7247	Melanterite	H14 Fe1 O11 S1		2					1										0.19
20	98-002-1503	Barite high	Ba1 O4 S1			1	1													0.13
21	98-001-7371	Galena	Pb1 S1		1															0.06
22	98-005-6956	Phengite 3T	H1.2 Al1.4 F0.8 Fe0.04 K1 Mg0.75 O11.2 Si3.81		1															0.06
23	98-002-8127	Ankerite	C2 Ca0.997 Fe0.676 Mg0.273 Mn0.054 O6						1											0.06
24	98-002-2570	Halite, bromian	Br0.1018 Cl0.8982 Na1															1		0.06

Appendix C

Table A3. XRD analyses of representative samples from alteration zone-2 (calcite–epidote–albite ± chlorite ± sericite).

No.	Ref. Code	Compound Name	Chemical Formula	SemiQuant [%]											Average
				H4	H10	H16	H17	H19	H23	H27	H29	H30	H32	H41	
1	98-004-6436	Albite low	Al1.005 Na0.986 O8 Si2.995	29	26	14	31	16	19	11	16	16	29	16	20.3
2	98-005-4829	Quartz low	O2 Si1	26	7	21	10	12	18	17	8	8	16	38	16.5
3	98-004-5914	Muscovite 2M1	H2 Al2.9 K1 O12 Si3.1	31	13	2	9	13	17	4	12	1	2	5	9.9
4	98-003-4690	Clinochlore IIb-4	H8 Al1.7 Fe0.33 Mg4.95 O18 Si3.02	12	10	14	12	11	7	5	17	14	5		9.7
5	98-001-7363	Microcline	Al1 K1 O8 Si3		10	9	8	11	9	7	7	7	16	12	8.7
6	98-005-2473	Sericite 2M1	Al2.724 Ca0.011 Fe0.032 K0.776 Mg0.022 Na0.181 O11 Si3.148 Ti0.02			8	6		9	28	8		22		7.4
7	98-001-8053	Anorthite	Al2 Ca1 O8 Si2					15		10	20	20		12	7.0
8	98-001-2962	Kaolinite 1A	H4 Al2 O9 Si2		6	15				5	12	14	8	3	5.7
9	98-005-7051	Illite 2M1	H3 Al4 K1 O12 Si2		20			18							3.5
10	98-004-5295	Chlorite IIb+4, chromian	H8 Al1.75 Cr0.25 Mg5 O18 Si3			14			18						2.9
11	98-006-0995	Calcite	C1 Ca1 O3			1	1		2		6	13	2		2.3
12	98-001-1876	Lepidolite 6M	H1 Al1 F1 K1 Mg3 O11 Si3							13				9	2.0
13	98-001-7534	Orthoclase	Al1 K1 O8 Si3		9		7								1.5
14	98-003-7636	Chamosite 1MIIb	H16 Al5.024 Fe4.964 Mg5.036 O36 Si5.7				9								0.8
15	98-002-2747	Titanite	Ca1 O5 Si1 Ti1											5	0.5
16	98-001-2031	Epidote	H1 Al2 Ca2 Fe1 O13 Si3				6								0.5
17	98-005-0411	Dolomite	C2 Ca1 Mg1 O6	1				1							0.2
18	98-001-2313	Phlogopite 3T	H1 Al1 F1 K1 Mg3 O11 Si3	2											0.2
19	98-000-6129	Bornite	Cu4.98 Fe1.02 S4		1										0.1
20	98-007-0040	Hematite	Fe2 O3					1							0.1
21	98-004-1521	Magnetite	Fe3 O4					1							0.1
22	98-003-8836	Phengite 3T	H2 Al1.848 K1 Mg0.58 O12 Si3.572						1						0.1
23	98-001-7325	Gypsum	H4 Ca1 O6 S1								1				0.1
24	98-002-8130	Ankerite	C2 Ca0.997 Fe0.676 Mg0.273 Mn0.054 O6											1	0.1

References

1. Rose, A.W.; Burt, D.M. Hydrothermal alteration. In *Geochemistry of Hydrothermal Ore Deposits*, 3rd ed.; Barnes, H.L., Ed.; John Wiley & Sons: New York, NY, USA, 1979; pp. 173–227.
2. Meyer, C.; Hemley, J.J. Wall rock alteration. *Geochem. Hydrothermal Ore Depos.* **1967**, *1*, 166–235.
3. Creasey, S.C. Some phase relations in the hydrothermally altered rocks of porphyry copper deposits. *Econ. Geol.* **1959**, *54*, 351–373. [CrossRef]
4. Lowell, J.D.; Guilbert, J.M. Lateral and Vertical Alteration-Mineralization Zoning in Porphyry Ore Deposits. *Econ. Geol.* **1970**, *65*, 373–408. [CrossRef]

5. Beane, R.; Bodnar, R. Hydrothermal fluids and hydrothermal alteration in porphyry copper deposits: Arizona Geological Society Digest. *Porphyry Copp. Depos. Am. Cordill.* **1995**, *20*, 83–93.
6. Sabins, F.F. Remote sensing for mineral exploration. *Ore Geol. Rev.* **1999**, *14*, 157–183. [CrossRef]
7. Watanabe, Y.; Hedenquist, J.W. Mineralogic and stable isotope zonation at the surface over the El Salvador porphyry copper deposit, Chile. *Econ. Geol.* **2001**, *96*, 1775–1797. [CrossRef]
8. Seedorff, E.; Dilles, J.H.; Proffett, J.M.; Einaudi, M.T.; Zurcher, L.; Stavast, W.J.; Johnson, D.A.; Barton, M.D. Porphyry deposits: Characteristics and origin of hypogene features. *Econ. Geol.* **2005**. [CrossRef]
9. Sillitoe, R.H. Porphyry copper systems. *Econ. Geol.* **2010**, *105*, 3–41. [CrossRef]
10. Tayor, H. The application of oxygen and hydrogen isotope studies to problems of hydrothermal alteration and ore deposit. *Econ. Geol.* **1974**, *69*, 843–883.
11. Gustafson, L.B.; Hunt, J.P. The porphyry copper deposit at El Salvador, Chile. *Econ. Geol.* **1975**, *70*, 857–912. [CrossRef]
12. Ohmoto, H. Stable isotope geochemistry of ore deposits. *Rev. Mineral. Geochem.* **1986**, *16*, 491–559.
13. Bowman, J.; Parry, W.; Kropp, W.; Kruer, S. Chemical and isotopic evolution of hydrothermal solutions at Bingham, Utah. *Econ. Geol.* **1987**, *82*, 395–428. [CrossRef]
14. Norman, D.; Parry, W.; Bowman, J.R. Petrology and geochemistry of propylitic alteration at Southwest Tintic, Utah. *Econ. Geol.* **1991**, *86*, 13–28. [CrossRef]
15. Dilles, J.H.; Solomon, G.C.; Taylor, H.P.; Einaudi, M.T. Oxygen and hydrogen isotope characteristics of hydrothermal alteration at the Ann-Mason porphyry copper deposit, Yerington, Nevada. *Econ. Geol.* **1992**, *87*, 44–63. [CrossRef]
16. Clark, A. Are outsize porphyry copper deposits either anatomically or environmentally distinctive? In *Giant Ore Deposits*; Society of Economic Geologists: Littleton, CO, USA, 1993.
17. Zaluski, G.; Nesbitt, B.; Muehlenbachs, K. Hydrothermal alteration and stable isotope systematics of the Babine porphyry Cu deposits, British Columbia; implications for fluid evolution of porphyry systems. *Econ. Geol.* **1994**, *89*, 1518–1541. [CrossRef]
18. Wilson, A.J.; Cooke, D.R.; Harper, B.J.; Deyell, C.L. Sulfur isotopic zonation in the Cadia district, southeastern Australia: Exploration significance and implications for the genesis of alkalic porphyry gold-Copper deposits. *Miner. Depos.* **2007**, *42*, 465–487. [CrossRef]
19. Urqueta, E.; Kyser, T.K.; Clark, A.H.; Stanley, C.R.; Oates, C.J. Lithogeochemistry of the Collahuasi porphyry Cu–Mo and epithermal Cu–Ag (–Au) cluster, northern Chile: Pearce element ratio vectors to ore. *Geochem. Explor. Environ. Anal.* **2009**, *9*, 9–17. [CrossRef]
20. Lentz, D.R. Exchange reactions in hydrothermally altered rocks: Examples from biotite-bearing assemblages. Alteration and alteration processes associated with ore-forming systems. *Geol. Assoc. Can. Short Course Notes* **1994**, *11*, 69–99.
21. Reed, M.H. Hydrothermal alteration and its relationship to ore fluid composition. *Geochem. Hydrothermal Ore Depos.* **1997**, *3*, 303–365.
22. Schwartz, G.M. Hydrothermal alteration. *Econ. Geol.* **1959**, *54*, 161–183. [CrossRef]
23. Pirajno, F. *Hydrothermal Processes and Mineral Systems*, 1st ed.; Springer: Heidelberg, Germany, 2009; p. 1250.
24. Gifkins, C.; Herrmann, W.; Large, R.R. *Altered Volcanic Rocks: A Guide to Description and Interpretation*; Centre for Ore Deposit Research, University of Tasmania: Hobart, Australia, 2005.
25. Janković, S. The copper deposits and geotectonic setting of the Thethyan Eurasian metallogenic belt. *Miner. Depos.* **1977**, *12*, 37–47. [CrossRef]
26. Altiner, D.; Kocyigit, A.; Farinacci, A.; Nicosia, U.; Conti, M. Jurassic-Lower Cretaceous stratigraphy and paleogeographic evolution of the southern part of north-western Anatolia (Turkey). *Geol. Romana* **1991**, *27*, 13–80.
27. Yigit, O. Mineral deposits of Turkey in relation to Tethyan metallogeny: Implications for future mineral exploration. *Econ. Geol.* **2009**, *104*, 19–51. [CrossRef]
28. Krushensky, R.; Akcay, Y.; Karaege, E. *Geology of the Karalar-Yesiler Area, Northwest Anatolia, Turkey*; US Geological Survey: Reston, VA, USA, 1974; pp. 1258–2331.
29. Şengör, A.C.; Yilmaz, Y. Tethyan evolution of Turkey: A plate tectonic approach. *Tectonophysics* **1981**, *75*, 181–241. [CrossRef]
30. Şengör, A.; Yılmaz, Y.; Sungurlu, O. Tectonics of the Mediterranean Cimmerides: Nature and evolution of the western termination of Palaeo-Tethys. *Geol. Soc. Lond. Spec. Publ.* **1984**, *17*, 77–112. [CrossRef]
31. Carr, M. *Igpet 2007 for Windows XP or Vista*, Terra Softa Inc.: Newark, NJ, USA, 2007.
32. Coelho, J. GEOISO—A Windows™ program to calculate and plot mass balances and volume changes occurring in a wide variety of geologic processes. *Comput. Geosci.* **2006**, *32*, 1523–1528. [CrossRef]
33. Gresens, R.L. Composition-Volume relationships of metasomatism. *Chem. Geol.* **1967**, *2*, 47–65. [CrossRef]
34. Grant, J.A. The isocon diagram; a simple solution to Gresens' equation for metasomatic alteration. *Econ. Geol.* **1986**, *81*, 1976–1982. [CrossRef]
35. Grant, J.A. Isocon analysis: A brief review of the method and applications. *Phys. Chem. Earth Parts A/B/C* **2005**, *30*, 997–1004. [CrossRef]
36. Herron, M.M. Geochemical classification of terrigenous sands and shales from core or log data. *J. Sediment. Res.* **1988**, *58*, 820–829.
37. Taylor, S.R.; McLennan, S.M. *The Continental Crust: Its Composition and Evolution*; Blackwell Scientific Publications: Hoboken, NJ, USA, 1985.

38. Floyd, P.; Leveridge, B. Tectonic environment of the Devonian Gramscatho basin, south Cornwall: Framework mode and geochemical evidence from turbiditic sandstones. *J. Geol. Soc.* **1987**, *144*, 531–542. [CrossRef]
39. van de Kamp, P.C.; Leake, B.E.; Senior, A. The petrography and geochemistry of some Californian arkoses with application to identifying gneisses of metasedimentary origin. *J. Geol.* **1976**, *84*, 195–212. [CrossRef]
40. Condie, K.C.; Macke, J.E.; Reimer, T.O. Petrology and geochemistry of early Precambrian graywackes from the Fig Tree Group, South Africa. *Geol. Soc. Am. Bull.* **1970**, *81*, 2759–2776. [CrossRef]
41. Caby, R.; Dostal, J.; Dupuy, C. Upper Proterozoic volcanic graywackes from northwestern Hoggar (Algeria)—Geology and geochemistry. *Precambrian Res.* **1977**, *5*, 283–297. [CrossRef]
42. van de Kamp, P.C. Geochemistry and origin of metasediments in the Haliburton-Madoc area, southeastern Ontario. *Can. J. Earth Sci.* **1968**, *5*, 1337–1372. [CrossRef]
43. Roser, B.; Korsch, R. Determination of tectonic setting of sandstone-Mudstone suites using content and ratio. *J. Geol.* **1986**, *94*, 635–650. [CrossRef]
44. Bhatia, M.R. Plate tectonics and geochemical composition of sandstones. *J. Geol.* **1983**, *91*, 611–627. [CrossRef]
45. Ishikawa, Y.; Sawaguchi, T.; Iwaya, S.; Horiuchi, M. Delineation of prospecting targets for Kuroko deposits based on modes of volcanism of underlying dacite and alteration halos. *Min. Geol.* **1976**, *26*, 105–117.
46. Williams, N.C.; Davidson, G.J. Possible submarine advanced argillic alteration at the Basin Lake prospect, Western Tasmania, Australia. *Econ. Geol.* **2004**, *99*, 987–1002. [CrossRef]
47. Large, R.R.; Gemmell, J.B.; Paulick, H.; Huston, D.L. The alteration box plot: A simple approach to understanding the relationship between alteration mineralogy and lithogeochemistry associated with volcanic-hosted massive sulfide deposits. *Econ. Geol.* **2001**, *96*, 957–971. [CrossRef]
48. Sánchez-España, J.; Velasco, F.; Yusta, I. Hydrothermal alteration of felsic volcanic rocks associated with massive sulphide deposition in the northern Iberian Pyrite Belt (SW Spain). *Appl. Geochem.* **2000**, *15*, 1265–1290. [CrossRef]
49. Kumral, M.; Abdelnasser, A.; Budakoglu, M. Geochemistry of Hydrothermal Alteration Associated with Cenozoic Intrusion-Hosted Cu-Pb-Zn Mineralization at Tavşanlı Area, Kütahya, NW Turkey. *Minerals* **2016**, *6*, 13. [CrossRef]
50. Large, R.R. Australian volcanic-Hosted massive sulfide deposits; features, styles, and genetic models. *Econ. Geol.* **1992**, *87*, 471–510. [CrossRef]
51. Ohmoto, H.; Rye, R. Isotopes of sulfur and carbon. *Geochem. Hydrothermal Ore Depos.* **1979**, 509–567.
52. Czamanske, G.K.; Rye, R.O. Experimentally determined sulfur isotope fractionations between sphalerite and galena in the temperature range 600 degrees to 275 degrees C. *Econ. Geol.* **1974**, *69*, 17–25. [CrossRef]
53. Chaussidon, M.; Lorand, J.-P. Sulphur isotope composition of orogenic spinel lherzolite massifs from Ariege (North-Eastern Pyrenees, France): An ion microprobe study. *Geochim. Et Cosmochim. Acta* **1990**, *54*, 2835–2846. [CrossRef]
54. McCuaig, T.C.; Kerrich, R. P—T—t—deformation—fluid characteristics of lode gold deposits: Evidence from alteration systematics. *Ore Geol. Rev.* **1998**, *12*, 381–453. [CrossRef]
55. Rollinson, H. *Using Geochemical Data*; Cambridge University Press: Cambridge, UK, 1993; p. 352.
56. Richards, J.P. Alkalic-Type epithermal gold deposits—A review. In *Magmas, Fluids, and Ore Deposits, Mineralogical Association of Canada Short Course*; Mineralogical Association of Canada: Quebec, QC, Canada, 1995; Volume 23, pp. 367–400.
57. Ueda, A.; Sakai, H. Sulfur isotope study of Quaternary volcanic rocks from the Japanese Islands Arc. *Geochim. Et Cosmochim. Acta* **1984**, *48*, 1837–1848. [CrossRef]
58. Chaussidon, M.; Albarede, F.; Sheppard, M. Sulphur isotope heterogeneity in the mantle from ion microprobe measurements of sulphide inclusions in diamonds. *Nature* **1987**, *330*, 242–244. [CrossRef]
59. Rye, R.; Luhr, J.; Wasserman, M. Sulfur and oxygen isotopic systematics of the 1982 eruptions of El Chichón Volcano, Chiapas, Mexico. *J. Volcanol. Geotherm. Res.* **1984**, *23*, 109–123. [CrossRef]
60. Luhr, J.F.; Logan, M.A.V. Sulfur isotope systematics of the 1982 El Chichón trachyandesite: An ion microprobe study. *Geochim. Et Cosmochim. Acta* **2002**, *66*, 3303–3316. [CrossRef]
61. Sasaki, A.; Ishihara, S. Sulfur isotopic composition of the magnetite-series and ilmenite-series granitoids in Japan. *Contrib. Mineral. Petrol.* **1979**, *68*, 107–115. [CrossRef]
62. Ishihara, S.; Sasaki, A. Sulfur isotopic ratios of the magnetite-series and ilmenite-series granitoids of the Sierra Nevada batholith—a reconnaissance study. *Geology* **1989**, *17*, 788–791. [CrossRef]
63. Santosh, M.; Masuda, H. Reconnaissance oxygen and sulfur isotopic mapping of Pan-African alkali granites and syenites in the southern Indian Shield. *Geochem. J.* **1991**, *25*, 173–185. [CrossRef]
64. Hoefs, J. Isotope fractionation processes of selected elements. In *Stable Isotope Geochemistry*; Springer: Berlin/Heidelberg, Germany, 2015; pp. 47–190.
65. Rudnick, R.; Gao, S.; Holland, H.; Turekian, K. Composition of the continental crust. *Crust* **2003**, *3*, 1–64.